THE UNIVERSITY OF CHICAGO

DETERMINATION OF THE VOLUMETRIC TYPE IA SUPERNOVA RATE USING THE FULL 5 YEAR DARK ENERGY SURVEY PHOTOMETRICALLY CLASSIFIED SAMPLE

A DISSERTATION SUBMITTED TO
THE FACULTY OF THE DIVISION OF THE PHYSICAL SCIENCES
IN CANDIDACY FOR THE DEGREE OF
DOCTOR OF PHILOSOPHY

DEPARTMENT OF ASTRONOMY AND ASTROPHYSICS

BY
JAMES LASKER

CHICAGO, ILLINOIS
DECEMBER 2020

Dedicated to the late Dr. Harold Lasker, who is out there smiling somewhere now that his son is also Dr. Lasker.

TABLE OF CONTENTS

LIST OF FIGURES

LIST OF TABLES

ACKNOWLEDGMENTS

First of all, I want to thank both of my advisors Josh Frieman and Rick Kessler for their invaluable wisdom and infinite patience. I would like to specifically thank Josh for his drive which helped push me to complete this analysis and Rick for his amazing attention to detail and development of the SNANA codebase which enabled this and countless other supernova analyses. I would also like to thank my committee, Daniel Fabrycky, Wendy Freedman, and Steve Kent for their feedback and advice on this thesis and analysis.

I also want to thank my grad school cohort and officemates, Phil Mansfield, Jason Poh, and Gourav Khullar for their comments on this thesis and accompanying presentation, as well as many years of discussion of research, teaching, outreach, python, and softball among other things. Having served as the captain of the department softball team, Little Bingo, for several years, I would be remiss if I did not mention them for helping provide an outlet for the stress of grad student life.

I was blessed with many amazing teachers before graduate school, and while there are far too many to mention here, I would like to highlight my middle school and high school Science Olympiad Head Coaches, Mrs. Adrianna Kenefick and Bro. Nigel Pratt S.M. All of the Science Olympiad coaches enabled me to explore my love of science in a highly motivating competitive environment. Additionally, I would like to thank Profs. Ponzy Lu and Masao Sako for enabling me to perform research in astronomy at an advanced level while still an undergraduate.

Finally, and most importantly, I would like to thank my family, especially my mother and late father without whom I would literally not be here and my sister whom I love very much. Their love and support has enabled me to withstand the immense stress of graduate school and the completion of this analysis.

ABSTRACT

In this thesis, I present a measurement of the volumetric type Ia Supernova (SN Ia) rate from the full 5-year supernova sample from the Dark Energy Survey (DES), the first scientific analysis using this sample. After applying selection criteria to the DES-SN light curves designed to achieve a relatively pure and complete sample of high-quality SN Ia events, the resulting sample comprises 2077 photometrically classified SNe Ia over the redshift range 0.1 to 0.9, the largest homogeneously selected sample in this redshift range. Based on simulations of the DES-SN sample, adjusted so that the tails of the distribution of the residuals in the supernova Hubble diagram match those of the data, I estimate the contamination of the selected sample from core-collapse SNe is 7.8% and correct the SN Ia rate accordingly. This is the first rate analysis to use only photometric supernova information, not relying on spectroscopic SN typing, spectroscopic SN redshifts, or any host information including spectroscopic and photometric redshifts. This kind of analysis is necessary to utilize the full statistical power of the DES-SN sample and will become more critical with the arrival of the Vera Rubin Observatory's (VRO) Legacy Survey of Space and Time (LSST) and its immense supernova sample ($\sim 100,000$). In order to demonstrate that this kind of analysis is viable, I validate the photometric redshift fitting and photometric classification code on simulations, using spectroscopic information that is otherwise not used in the analysis. As in previous SN Ia rate analyses (1; 2; 3), I find that the volumetric SN Ia rate is consistent with ($\chi^2 = 13.95$, 6 DOF) a power-law form, $R(z) = k(1+z)^{\beta}/\mathrm{yr}/\mathrm{Mpc}^3$ over the redshift range 0.1 to 0.9 and obtain k= 2.00 ± 0.21 (stat) ± 0.24 (sys) x 10^{-5} and $\beta = 1.82$ ± 0.23 (stat) ± 0.31 (sys) using only DES data and a result of k = 2.03 ± 0.19 (stat) ± 0.18 (sys) x 10^{-5} and $\beta = 1.79$ ± 0.20 (stat) ± 0.27 (sys) when adding a prior from an SDSS rate analysis to anchor the rate at low redshift. Both of these results are consistent with measurements from prior rate analyses, and they improve the statistical errors on parameters from single-survey analyses while being the first to add a systematic error analysis for their power law rate results. The analysis was performed in a blinded fashion, obscuring the exact

value of the rate parameters until the analysis was finalized to prevent such consistency from being forced by analysis choices. The systematic errors in the rate parameters are estimated by varying a number of selection parameters that impact sample purity and completeness (in both the simulations and the data sample), varying the simulation core collapse model, and changing the redshift range considered in the analysis. This data sample will be used in a future analysis to measure a delay time distribution between star formation and SN Ia explosion and constrain SN Ia progenitor models.

CHAPTER 1

INTRODUCTION

From the earliest observations of type Ia supernovae, it has been suspected that they might have a standard peak luminosity that could be utilized in cosmological distance measurements (4; 5; 6; 7; 8; 9; 10; 11). Subsequent work by Phillips 1993 (12) building on the work of Pskovskii (13; 14; 15) was able to standardize the distance measurements based on decline rate. Then Tripp 1998 (16) standardized the distance measurements based on supernova color to a precision equal to the photometric measurement precision of the time. This standardization enabled precise cosmology measurements from the High-Z Supernova team (17; 18) and the Supernova Cosmology Project (19) who used distances measured using those methods to discover the accelerating expansion of the universe. Since then, a number of surveys including the Sloan Digital Sky Survey (SDSS2, (20; 21)), Supernova Legacy Survey (SNLS, (22)), Panoramic Survey Telescope and Rapid Response System Supernova Survey (PS1, (23)), and, most recently, the Dark Energy Survey (DES, (24)) have expanded the sample size, redshift range, and measurement precision of type Ia Supernovae (SNe Ia) in the process of making more precise measurements of cosmological parameters. In parallel with those large surveys, recent HST measurements such as the Riess et al. 2016 (25) Cepheid observations, and Freedman et al. 2019 (26) measurements of the tip of the red giant branch have further been used to standardized supernovae on an absolute scale. In coming years, the space-based Wide Field Infrared Survey Telescope Survey (WFIRST, (27)) will extend the redshift range of SN Ia measurements beyond $z \sim 1$ and the ground-based LSST (28; 29) will increase the number of observed SNe Ia from a few thousand to potentially a quarter of a million. Despite this widespread usage of type Ia supernovae for cosmological distance measurements, we do not have a detailed understanding of SN Ia explosion mechanism(s) and progenitor system(s) and therefore do not have a physical explanation for why they are such good standardizable candles or whether they may fail to be completely standardizable candles.

Measurement of the evolution of the SN Ia rate with redshift, when combined with information about cosmic star formation history, can help to distinguish between proposed SN Ia progenitor models. This information is used to estimate the distribution of the delay times between star formation and supernova explosion. Since the proposed progenitor models make predictions about the delay time distribution (DTD) and those distributions differ substantially between models, a measurement of the DTD will distinguish between those models. In this thesis I focus on the SN Ia rate measurement and in a future publication, I will use this information to measure the DTD. The SN Ia rate is also an important piece of input information for the cosmology analysis of DES, which bases its analysis and bias corrections on simulations of the survey, and also for forecasts of future surveys like LSST.

In this thesis, I present the first measurement of the cosmological volumetric SN Ia rate with the DES sample. In this introduction I describe the leading theories for SN Ia progenitors and their predictions which have been tested through spectrophotometric observation and DTD measurements. I also describe the history of supernova rate analyses from modern sky surveys. In chapter 2, I will describe the Dark Energy Survey including its Supernova Survey along with the definition of the data sample used in this analysis . In chapter 3, I will describe the formalism I use to determine the rate. In chapter 4, I describe the simulations which are both used as parts of the mainline analysis and as parts of systematic tests of the analysis. In chapter 5 I report my results, and discuss impacts of different systematic tests on the sample characteristics and results.

1.1 Supernova Progenitor Systems

The primary three channels currently theorized for the formation of SNe Ia are Single Degenerate (SD, (30)) Core Degenerate (CD,(31)) and Double Degenerate (DD, (32), (33), (34)). The SD channel hypothesizes that one white dwarf accretes matter from a non-degenerate companion (usually a main sequence or red giant star) until its interior reaches the temperature for carbon fusion. The fusion of carbon then results in the thermonuclear detonation of the star into a supernova. The CD channel occurs during the common envelope phase of evolution of a WD-AGB binary system. In that case, the WD merges with the CO core of the AGB star before the common envelope disperses, causing the explosion. The DD channel requires two white dwarfs to be orbiting in a close binary. They then slowly spiral in towards each other due to their emission of gravitational radiation. Then, in some models the two WDs merge together or collide in order to cause the thermonuclear detonation of the combined system, and in others one WD is tidally disrupted and its mass begins to accrete onto its companion until detonation occurs. There are also variants of the Double Degenerate scenario where a DD system is part of a triple star system and the third star drives the merger of the DD system (35).

While these scenarios are independent channels for the formation of SNe Ia, any individual scenario or combination of scenarios could contribute to the observed SN Ia population. However, any combination of progenitor systems must still be able to account for the very narrow observed spread in peak SN Ia luminosities even before standardization, 0.25 mag found by Phillips et al. 1999 (36) before standardization and 0.09 mags of intrinsic scatter found post standardization in the DES-SN 3 year cosmology analysis (DES Collaboration 2019 (37)). The primary driver of SN Ia peak luminosity is ^{56}Ni decay and therefore these models must be able to also reproduce a narrow range of ^{56}Ni of order 0.4 to 0.7 $M_\odot$ as found by Dhawan et al. 2016 (38).

Livio and Mazzali 2018 (39) § 3 is an excellent review of the current state of knowledge of the supernova progenitor systems described above whose structure I follow here:

1.1.1 Single Degenerate Scenario

As first proposed by Whelan and Iben 1973 (30), the SD channel involves a white dwarf (WD) accreting mass from a main sequence star until it reaches the Chandrasekhar limit and carbon fusion results in the detonation of the WD into an SN Ia. Since this process is slow and relatively uniform and also results in explosion at a nearly constant mass, it would explain the usage of SNe Ia as standardizable candles. We also have observed enough systems composed of a WD and a non-degenerate companion which is funneling mass onto the WD at a rate which would cause it to reach the Chandrasekhar limit in less than a Hubble time to account for the observed SN Ia rate if the SD channel is the primary and/or only channel of SN Ia formation (Livio and Mazzali 2018 §3.2.1.2 (39)).

Observational evidence in favor of the SD channel primarily consists of evidence of interactions of the supernova explosion that is consistent with the presence of a companion star and CSM (40; 41; 42; 43; 44). The Single Degenerate model is also the subject of detailed simulations which show that it produces the ^{56}Ni mass necessary to match observed SN Ia luminosities(45).

Despite the aforementioned circumstantial evidence in favor of the existence of a companion MS star as predicted by the SD model, no such star has ever been observed(46; 47; 48; 49). This includes observations of very old and very nearby SNe Ia such as Tycho's SNR and SN2011fe where we can place tight constraints on the size of any unobserved surviving companion. Several theories of SD SNe Ia that allow for the lack of an observable companion star predict emission outside the optical that has not been found (50; 51; 52; 53). In addition, several of the observations of interaction with CSM cited above were not repeated in other well-observed nearby SNe Ia (54; 55).

Finally, and most relevant to rate analyses, the SD model does not naturally produce the observed delay time distribution, proportional to t^{-1}, between star formation rate and supernova explosion rate. The SD scenario produces a large range of DTDs which are highly dependent on the stellar population synthesis code which is used, leading to a wide range of possible DTDs (56; 57).

Overall, the SD scenario is believed to account for at most a minority ($\leq 10\%$) of all SNe Ia (Soker 2020 (58)) with another recent analysis (Tucker et al. 2020 (55)) placing separate upper limits on a standard Hydrogen star companion below 5.5% and limits on a Helium star companion below 6.4% of all SNe Ia.

1.1.2 Core Degenerate Scenario

Similarly to the SD scenario, the CD scenario progenitor occurs as a natural outcome of binary star evolution. Observed close WD-WD binaries must all pass through an evolutionary stage where one of the stars is already a white dwarf and the other is an AGB star. During this phase, the AGB star's outer envelope expands and envelopes the WD, creating a common envelope evolution stage. In the configurations that produce WD-WD binaries, the common envelope is ejected before the WD and the core of the AGB star can merge. However, Livio and Riess 2003 (31) proposed that the WD and core of the AGB star can merge inside of the common envelope to produce a supernova in a method analogous to that of a DD while allowing the supernova explosion to interact with the common envelope.

The primary evidence in favor of the CD scenario includes the existence of a subclass of SN Ia with strong evidence of CSM interaction (SN Ia-CSM), accompanied by the complete lack of CSM interaction in the remainder of SN Ia. If the SD scenario produced most of the SNe Ia, then there would be a continuum of CSM interaction that was observed based on, among other things, stellar wind rate for the non degenerate companion. This would also explain why no evidence of a companion star as predicted by the SD model has yet been found.

An analysis by Bear and Soker 2018 (59) found that in order to support the estimated SN Ia rate in the Milky Way via the CD model, roughly 0.2% of all WDs must have masses $\geq 1.35 M_\odot$, which they describe as "waiting to explode" under the CD model. Though they note large uncertainties, their catalog analysis suggests 1-3% of MW WDs are $\geq 1.35 M_\odot$ which suggests the validity of the CD model from a progenitor availability standpoint. They do not, however, present new evidence for its validity in any particular case.

While not explicitly evidence against the CD model, there is a lack of simulations detailing the model's progression. Aznar-Siguán et al. 2015 (60) have shown that common envelope evolution can produce a merger for several core temperature values, disc masses, and orbital parameters. However, they do not simulate the actual explosion and do not present any observable parameters such as light curves and nickel mass.

Lastly, and similarly to the SD model, the CD model does not naturally produce the observed delay time distribution, proportional to t^{-1}. Meng and Yang 2012 (61) note that the standard CD model only produces the shortest of observed delay times and cannot be the dominant source of SNe Ia. However, they use the spindown formalism of Ilkov and Soker 2012 (62) to show that for a normal range of initial magnetic field parameters, that the spindown time can create an observed DTD of $t^{-\beta}$ where β can be, but is not necessarily, the observed value of 1.

1.1.3 Double Degenerate Scenario

The DD scenario results from the gravitational radiation-induced inspiral of two CO WDs (Webbink 1984 (63); Iben & Tutukov 1984 (64)). Once the inspiral has shrunk the Roche lobe of the donor (larger) WD below its radius, it begins to transfer mass onto the central (smaller) WD. Since the size of degenerate systems increases with decreasing mass, this causes the donor WD to continue to grow until the mass loss timescale becomes comparable with the gravitational inspiral timescale. At that point, the donor WD is rapidly disrupted and either coalesces with the central WD or forms a disk around it. Once the mass gain from the accretion or coalescence causes part of the combined system to reach or surpass the carbon fusion temperature, carbon detonation occurs and an SN Ia is formed.

Similarly to the CD scenario, the DD scenario is a natural product of binary star evolution where the merger occurs after the common envelope phase and after the core of the AGB star has cooled and shrunk to become a WD. While many such systems have been observed, including, most recently, a sample of 39 reported by the Supernova Progenitor surveY (SPY, Napiwotzki et al. 2019 (65), there has not yet been an observed DD system with combined mass above the Chandrasekhar limit that will merge in less than a Hubble time. However, Rebassa-Mansergas et al. 2019 (66) suggest that this lack of detection is due to the intrinsic faintness of these systems and difficulty in extracting their double hydrogen line profiles.

They also suggest that such systems are highly unlikely to be detected before the advent of space-based gravitational wave observatories like LISA. There has also been evidence of SNe Ia with sub-Chandrasekhar ejecta mass(Scalzo et al. 2014, (67)), implying that the double degenerate progenitors need not have a combined mass over that limit.

While a DD scenario would not explain the small number of SNIa-CSM with Hydrogen present in their spectra or other indications of CSM interaction, it would explain why most SNe Ia do not have Hydrogen in their spectra and why none of the SNe Ia which have been observed in detail (see SD section above) show any indication of a surviving partner star.

One of the major pieces of evidence in favor of the DD model is that it naturally produces the t^{-1} DTD that is found in observations. The delay time distribution can be theoretically derived from the distribution of semimajor axes of the initial, post common envelope, white dwarf binary ($d\mathrm{N}/\mathrm{da} \sim a^{\epsilon}$) and the rate of decay of the initial orbit ($\mathrm{t} \sim a^{\gamma}$; $d\mathrm{a}/d\mathrm{t} \sim a^{1-\gamma}$) to be $d\mathrm{N}/d\mathrm{t} \sim a^{1-\frac{\epsilon+1}{\gamma}}$ (Yungelson & Kuranov 2017 (68)). Kraicheva et al. 1979 (69) found that data from Batten's catalog of spectroscopic binaries supported a distribution where ϵ = -1, implying that for any method of orbital decay (including GWR where $t \sim a^{-4}$)), the DTD is proportional to t^{-1}. Additionally, a recent analysis by Strolger et al. 2020 (57) reconstructed a DTD consistent with t^{-1} using a flexible skew-normal function that does not require an power law form.

One major problem with the standard DD scenario is that its standard variant results in an accretion induced collapse (AIC), where the primary WD accretes enough mass from the donor WD to trigger Oxygen/Neon burning rather than a carbon detonation to form a neutron star in an event much fainter than a supernova.

Another problem is that standard variants of the DD scenario produce supernovae that lack the spherical symmetry that has been observed in most SNe Ia, since mergers and collisions are inherently non-spherically symmetric. However, Soker 2020 (58) argues that a DD scenario with a delay of several dynamical timescales between the merger and explosion would allow for the product of the merger to become spherically symmetric.

In summary, the astrophysical evidence leans towards the DD scenario contributing a majority of observed SNe Ia. However, this evidence is not conclusive, with some analyses suggesting that multiple channels may account for different subtypes of SNe Ia or that multiple scenarios produce what we call normal SNe Ia. More precise measurements of the SN Ia rate can give us more insight into the evolution of the delay time distribution. Increased resolution in delay time and more precise measurements of the DTD could either show contributions from multiple channels to the normal SN Ia rate or help determine which subtypes of the DD scenario form SNe Ia.

1.2 Prior Sky Survey Rate Analyses

In this section I will give a brief history of the evolution of analyses of the volumetric type Ia SN Ia rate with redshift as measured by ground based surveys including the University of Hawaii's Institute for Astronomy (IfA) survey (70), Subaru Deep Field survey (71), Sloan Digital Sky Survey (SDSS) (1; 2), Supernova Legacy Survey (SNLS) (3), and Palomar Transient Factory (PTF) (72).

1.2.1 Prior Supernova Rate Analysis Samples and Results

The IfA survey was one of the first modern supernova surveys to conduct a rate analysis. Their sample consisted of 98 supernovae, 23 of which were spectroscopically-confirmed SNe Ia, between redshift 0.3 and 0.8. They calculated their rate by determining the "control time" for each observed supernova, i.e. the total time that the survey would have been able to observe each supernova it did observe as a function of redshift, peak magnitude, and explosion time, and weighting each supernova by the inverse of that time. They show that the rate is increasing with redshift and combine that fit with star formation rate information to find a relatively short delay time.

Relatively shortly afterwards, the Subaru deep field survey conducted its rate analysis.

Their sample consisted of 33 events below redshift 1.6 with all of the events they believed to be SNe Ia above redshift 0.5. Using photometric classification and a large simulation of many types of supernovae (Ia, Ibc, IIn, II-p), they estimated that their sample was only 55% SN Ia with core collapse contaminants accounting for the other 45%. The actual rate calculation proceeded very similarly to the IfA analysis, consisting of binning of the SNe into 4 bins ($\Delta z = 0.5$) and then adjusting their value for the "control time" as a function of redshift, magnitude, and survey properties. Their analysis, though with large errorbars, showed a slowly increasing rate at intermediate redshift like IfA but also showed a turnover at the highest redshifts.

SDSS conducted two similar rate analyses, the first of which (Dilday et al. 2008, (1)) was performed early on in the survey using a small subset of the final data and therefore did not have the statistical power or redshift coverage to measure the rate as a function of redshift on its own. The second, and final, SDSS rate analysis (Dilday et al. 2010, (2)) is one of the first analyses to leverage the size of a large photometrically classified sample of well-measured SN light curves to allow an accurate determination of a volumetric rate vs. redshift.

The Dilday et al. 2008 analysis was conducted on a very small subset of the SDSS data. 17 supernovae (16 spectroscopically confirmed, 1 photometric), at very low redshift ($z < 0.12$). They calculate their SDSS-only rate similarly to other surveys, by weighting their observed supernovae by a measure of the effective time and dividing volume covered by the survey adjusted for effects like pixel masking and the fake SN-measured detection efficiency. Due to the small sample size and redshift range, they report their results as a single rate at the effective redshift center of the data ($z = 0.09$).

Since this sample was only spectroscopically complete out to $z \sim 0.12$, they combined their sample with those of other rate analyses which used spectroscopically classified supernovae in order to find a trend of volumetric supernova rate vs. redshift. They fit this rate to a power law of $(1+z)^{\beta}$ using a maximum likelihood method over all of the samples. However due to the large systematics in combining 5 different samples as well as the still small total sample size and the incompleteness at intermediate redshifts, they were only able to detect an increasing supernova rate vs. redshift at a 2.5σ level.

The Dilday et al. 2010 (2) rate analysis was conducted after the end of the SDSS-II Supernova survey. As a result, they had both a much larger sample of spectroscopically confirmed SNe Ia (270) and a substantial photometrically classified sample (246). Among the photometrically classified events, 113 had host galaxy spectroscopic redshifts while the remainder used photometric redshifts, which were determined by adding the redshift as an additional fit parameter in the MLCS2k2 model (Kessler et al. 2010 (73)). First, they repeated the analysis in Dilday et al. 2008 out to z = 0.12 to find a local SN Ia rate consistent with the prior analysis. They also repeated that analysis using their sample out to z = 0.15 where the SN Ia rate could be taken to be approximately constant. Then, again repeating the prior analysis, but using only SDSS supernovae out to z = 0.3 and a power law form with the same redshift dependence, they fit the sample with an unbinned, maximum likelihood estimation. Their result is a better constraint on the $z < 0.12$ rate but a worse constraint on the power law index. It is not stated whether this is due to the lack of external data samples, photometric redshift uncertainties, or other factors.

The Dilday et al. 2010 analysis also estimates their Core Collapse contamination using the 87 spectroscopically confirmed CC-SNe discovered in SDSS. After putting them through the same pipeline and cuts as the SN Ia sample, they find a very low contamination fraction of either 0.02 or 0.03 depending on whether they use photometric or spectroscopic redshifts.

The SNLS rate analysis maintained the high data quality and sample size of the SDSS analyses while vastly expanding the redshift range out to z = 1.1. Perrett et al. 2012 (3) used 286 spectroscopically confirmed SNe Ia and a sample of 405 photometrically classified SNe Ia from SNLS. Between the events with spectra of the live SN and those with host galaxy redshifts, about half of all events have a spectroscopic redshift. They fit a rate in small redshift bins where $\Delta z = 0.1$ and while each rate has a larger uncertainty than prior low-redshift rates, the uncertainty on the power law index is improved over SDSS by a factor of 2. When they add in other data samples including SDSS and SNLS, the error drops to 1/5 that of SDSS on the power law index and it is 2/3 that on the normalization.

Recently, Frohmaier et al. 2019 (72) performed an excellent low-redshift rate analysis using the Palomar Transient Factory (PTF) data set. Their sample consisted of 90 SNe Ia, only 6 of which were photometrically classified, below a redshift of 0.09. Additionally, they combined their rate with measurements from SDSS, SNLS, Subaru (Graur et al. 2011 (74)), and CANDELS (Cosmic Assembly Near-infrared Deep Extragalactic Legacy Survey, Rodney et al. 2014 (75)) to fit a rate power law vs redshift. Both their published low-z rate and their cosmological rate power law are in agreement with prior rate analyses. They also measured several delay time distributions for various star formation history models which were all consistent with t^{-1} at the 1-σ (~ 0.1 in power law index) level as expected from the double degenerate scenario.

The results of the power law fits from these analyses can be found in Table 5.11.

1.2.2 Prior Supernova Rate Analysis Methodological improvements

While many of the improvements in the constraints on the rate measurements from the above analyses can be attributed to technological improvements, the methodology used to perform the analyses and surveys has improved as well.

The Ifa survey was one of the first surveys to conduct many successive observations of a single field in order to discover SNe and track their light curves. This survey used many methods that would be repeated and improved upon in future surveys and rate analyses. These include the usage of difference imaging to discover supernovae and measure their light curves, the usage of fake supernovae on images to measure their limiting magnitude and survey efficiency, and a template fitting method for light curve fitting.

The Subaru survey imaging was what, at the time, was more typical of a supernova survey: a template image followed up years afterwards by two deep discovery epochs on consecutive nights in multiple bands (R$i'z'$). They also took follow up data in unfiltered light on other instruments at later epochs in order to rule out multi-year variability and find fainter host galaxies.This resulted in a more pure supernova sample with better redshift information from hosts. Their detection efficiency and limiting magnitudes were also measured using fakes, but with a more detailed analysis based on the photometric redshifts of all field galaxies and the usage of the galaxy luminosity function to extrapolate fake placement to unobserved galaxies.

By the time of the SDSS supernova survey, the methodology of supernova surveys improved substantially. The SDSS supernova survey was part of the first generation of "rolling search" surveys, meaning that it repeatedly imaged a large area (SDSS Stripe 82) over the course of several years (2005-2007) obtaining a cadence of ≤ 4 days between observations in all five of the SDSS bands $ugriz$. These regular, but shorter, observations allow for excellent characterization of a much shallower sample than Subaru and IfA.

As for prior surveys, all of the photometry which led to SN discovery was performed via difference imaging. Also as in prior surveys, SDSS monitored its detection efficiency in real time using fake supernovae. The SDSS fake supernovae were drawn from a redshift distribution that increased only with survey volume and, after the first year, included an extinction parameter drawn from an exponential distribution. Then the single epoch detection efficiency from those fakes was used to simulate supernovae with realistic parameter distributions and measure efficiencies with respect to those parameters.

Due to their large photometric sample, Dilday et al. 2010 tested the bias on their rate measurement due to photometric redshift biases. To do this, they test the distribution of the differences between the photometric redshifts and their relatively large sample with spectroscopic redshifts of either hosts or supernovae. They find that the bias is small relative to their statistical and systematic errors both because of the large spectroscopic subsample and the small overall redshift bias.

SNLS also used difference imaging photometry to discover and measure supernova light curves. However, instead of modifying their spectroscopic light curve fitting code to fit for redshift like SNLS, they utilized a second code which was designed to fit a photometric supernova redshift. While this enables each code to be optimized for each subsample, it could introduce systematic errors when combining them into a single analysis.

The fake SN monitoring of the survey efficiency for SNLS was performed using 2.5 million fake SNe with a well-defined redshift and stretch sample (flat in redshift inside the survey range and flat in stretch between 0.5 and 1.3). As expected, blue, high stretch, and low redshift SNe are the most efficiently recovered. These efficiencies were then used in the rate analysis.

Like SNLS, PTF used millions of fake supernovae to determine their single epoch detection efficiency and then they simulated samples using that efficiency to determine their overall supernova detection efficiency. Their simulations were an improvement over those used by SNLS due to their incorporation of host surface brightness as a simulation parameter and their larger sample size of overlaid fake supernovae. Using this information, PTF created 56 separate efficiency grids based on SN and survey parameters for use in the analysis.

The DES rate measurement should improve on the most recent comparable rate measurement (SNLS) for several reasons. First are the many improvements in survey methodology and technology that allow for our increased sample size and quality. These include a larger field of view per field (2.7 square degrees vs. 1 square degree) which enables a larger overall survey area (27 square degrees vs. 4 square degrees), and a more sensitive camera, specifically in the redder bands, allowing higher signal to noise ratio at higher redshifts. Secondly, I am performing a detailed systematic analysis of my method to determine any errors not accounted for by the nominal analysis. None of the prior rate analyses have included such an analysis for their rate evolution measurements. Finally, I am using a purely photometric analysis with no spectroscopic typing or redshift information for supernovae or galaxies entering the rate analysis. While this may increase the apparent statistical error due to the inaccuracies in photometric redshift fitting, it will still result in a larger sample with greater statistical power.

CHAPTER 2

THE DARK ENERGY SURVEY SUPERNOVA SURVEY

The Dark Energy Survey (DES) included a 5000 deg^2 galaxy survey ("wide" survey) (76; 77) and a 27 deg^2, time domain, supernova survey (78; 79), which were run concurrently between August and February beginning in 2013 and ending in 2018. Only the wide survey continued operations from September 2018 to January 2019. The wide survey was conducted in 5 bands ($grizY$) of which the 4 bluest bands ($griz$) were used in the supernova survey. Survey observations were conducted on the Victor Blanco 4m telescope using the Dark Energy Camera (DECam) at the Cerro Tololo Interamerican Observatory (CTIO) in Chile.

DECam is a 570 Megapixel camera composed of 62 CCDs used for science plus 12 smaller CCDs used for guiding and focusing the telescope. DECam was constructed specifically for DES and has several properties which optimize it for the science goals of the survey. First is the large field of view, 2.7 square degrees, which enables the survey to tile a significant fraction ($\frac{1}{8}$) of the sky up to 10 times over the course of the survey. The CCDs themselves were also optimized for the survey, having a thickness of 250 μm. This allows for high efficiency in the redder bands which is necessary for observing red objects like highly redshifted galaxies and supernovae. See Figure 2.1[1] for the system throughput including atmospheric transmission function. This figure shows that the redder bands (i and z) have the highest throughput and that the throughput is over 80%. Figure 2.2 shows the DECam focal plane inside its mount and Figure 2.3 shows the alignment of the 62 science CCDs on the sky with a three-color composite image of the Fornax Cluster from first light.

The footprint for the wide-area survey was chosen to overlap with as much prior spectroscopic data, optical photometric data, and Sunyaev-Zeldovich cluster data as possible while staying in the region of the sky observable from CTIO between September and February and avoiding areas with high extinction or high stellar density near the galactic plane. The areas chosen for the survey included the footprint of the VISTA Hemisphere Survey (VHS) (80) to

---

[1] Figure from http://www.ctio.noao.edu/noao/node/13140

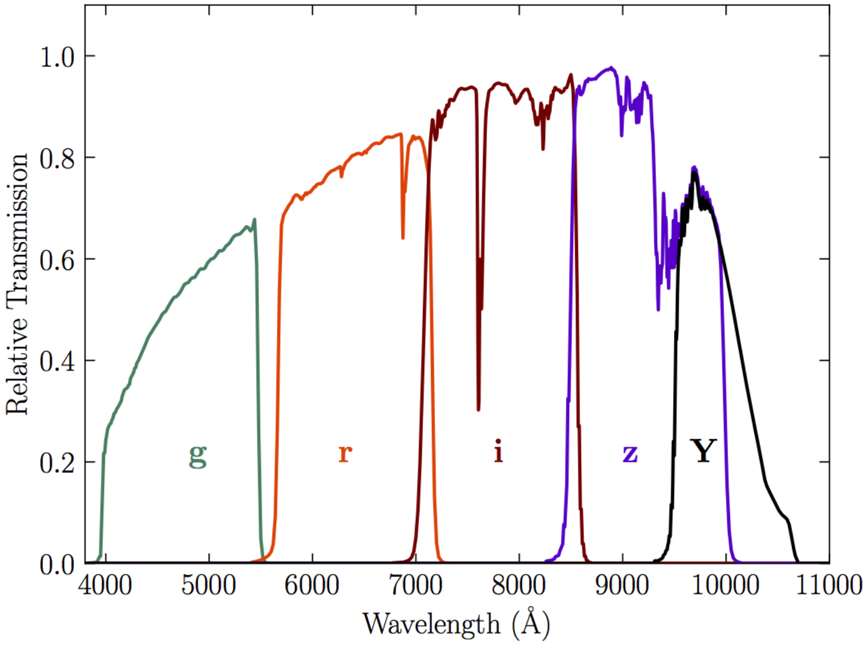

Figure 2.1: DECam average total system throughput including a model atmosphere at airmass = 1.2 in $grizY$ bands.

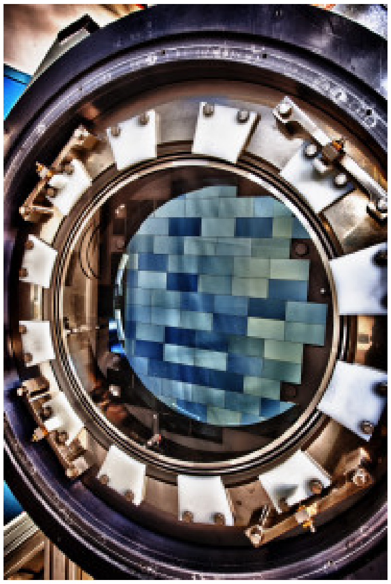

Figure 2.2: An image of the DECam focal plane with the 62 science CCDs visible as blue rectangles and the 12 guiding and focusing CCDs visible as blue squares.

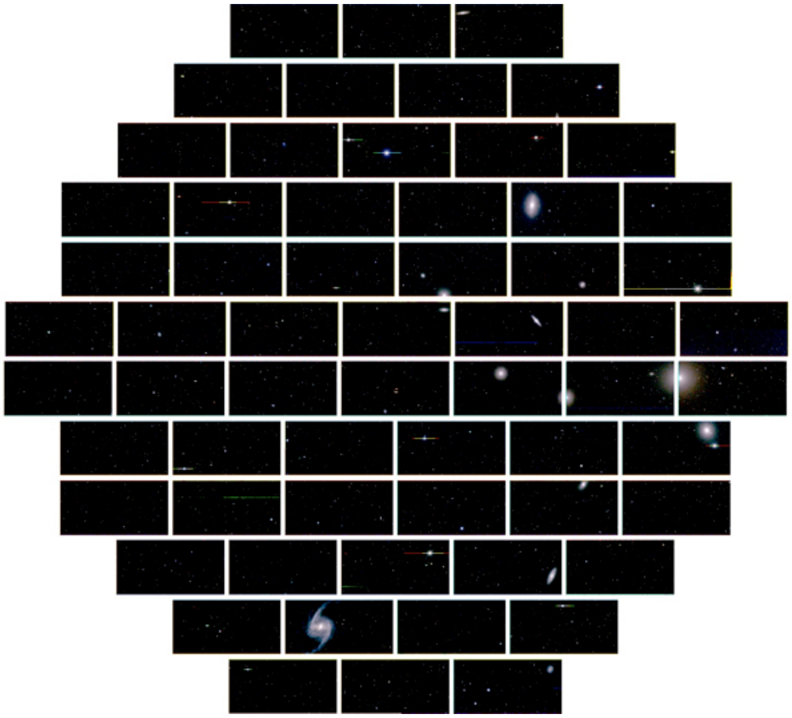

Figure 2.3: A composite 3-color image of the Fornax Cluster taken during DES first light.

use their IR data in photo-z measurements, the footprint of the South Pole Telescope (SPT) Survey (81) to utilize their SZ cluster mass estimates, SDSS Stripe 82 for its photometric calibration, and BOSS/eBOSS spectroscopic footprints to provide spectroscopic redshifts for galaxies as a training and test sample for the photometric redshift algorithms. The remainder of the footprint was chosen to connect the areas listed above while remaining distant from the galactic plane.

The 10 fields for the supernova survey were chosen in two parts. First a set of fields were chosen that were within the footprint for the wide survey, contained well observed patches of sky from prior surveys, and were observable from northern hemisphere 8-m class telescopes in order to obtain followup spectra of supernova candidates. These fields included ones which overlapped with SDSS stripe 82, the Chandra deep field south, the XMM Newton Large Scale Structure survey, the SNLS D1 field, and the ELAIS S1 field. Then, different survey strategies were simulated to select which subset of those fields and what exposure times would result in optimal constraints on cosmological parameters(82). The result of the

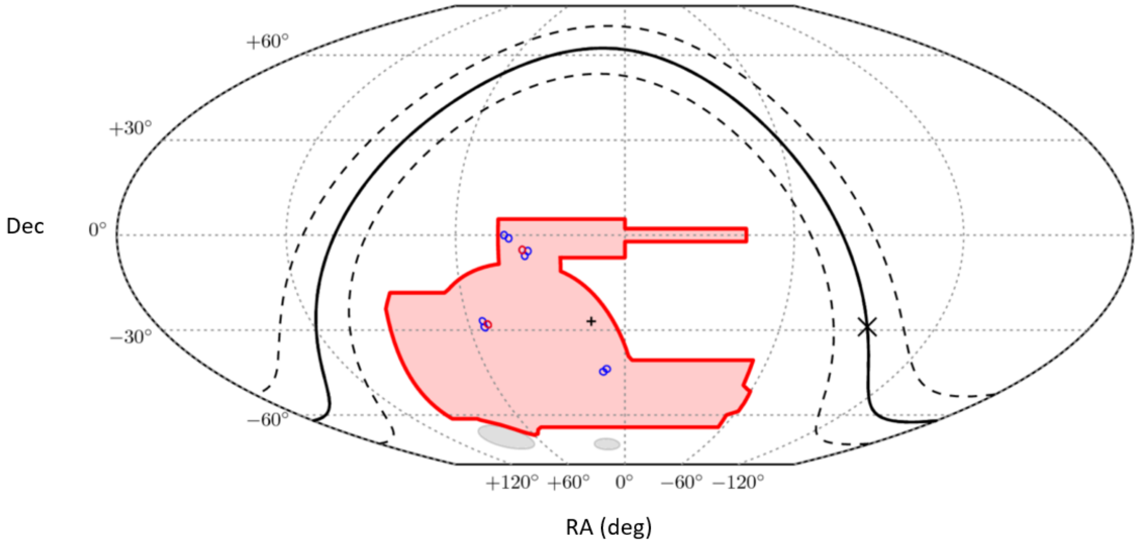

Figure 2.4: DES Footprint on sky is outlined in red. Supernova fields are circles in blue (shallow fields) or red (deep fields). The Galactic plane is shown as a black line and a 20 degree radius from the galactic plane is shown as parallel dotted lines. Grey dotted lines of constant Right Ascension (RA) run from top to bottom and grey dotted lines of constant declination run left to right. The "X" is the galactic center and the "+" is the South galactic pole

simulations was a "hybrid" strategy including 8 shallow (short exposure) and 2 deep (long exposure) fields (see Tables 2.1 and 2.2 for field location and exposure times).

The outline of the DES Footprint (red lines), shallow supernova fields (blue circles), and deep supernova field (red circles) are shown in Figure 2.4(DES Collaboration 2018, (83)).

The purpose of DES was to probe the origin of cosmic acceleration and the nature of dark energy using observations of weak gravitational lensing, galaxy clustering, baryon acoustic oscillations, and SNe Ia. The wide survey data is only used for the first three probes of cosmological parameters[2], so I will focus on the supernova survey.

2.1 The DES Supernova Survey and Data Sample

Having described DES in general, I will now describe the supernova survey in detail, focusing on several areas important to the rate analysis. These include the data collection, data

---

[2] This does not preclude the reprocessing of the wide field imaging data to discover supernovae.

Field	Depth	RA	Dec.
C1	Shallow	54.2743	-27.1116
C2	Shallow	54.2743	-29.0884
C3	Deep	52.6484	-28.1000
X1	Shallow	34.4757	-4.9295
X2	Shallow	35.6645	-6.4121
X3	Deep	36.4500	-4.6000
S1	Shallow	42.8200	0.0000
S2	Shallow	41.1944	-0.9884
E1	Shallow	7.8744	-43.0096
E2	Shallow	9.5000	-43.9980

Table 2.1: For each DES-SN field, lists whether it is shallow or deep, and the RA/DEC (degrees, J2000) coordinates of the field center.

processing, data analysis, and data sample definition.

The DES-SN survey is divided into 10 approximately 2.7 square degree fields which are grouped into 4 patches (see Figure 2.4) spread throughout the DES footprint. 2 of those 10 fields have significantly longer observations than the other 8 and are known as the "deep" fields. Observations of these deeper fields enable us to extend our observations to high redshifts (z $\sim$ 1.2). The 8 "shallow" fields enable us to monitor more area, and therefore discover more supernovae, at low to intermediate redshifts (z $\lesssim$ 0.7). Table 2.1 lists the depth and location of each field on the sky and Table 2.2 lists the exposure times for shallow fields and deep fields in each band along with the corresponding $5 - \sigma$ point source limiting magnitude. While all four bands of the shallow field observations are always taken consecutively on the same night, the deep field observations, due to their length, are taken on a band-by-band basis, not always on the same night. Information is taken from Kessler et al. 2015 and Smith et al. 2020(79; 84).

Observations of these supernova fields are interspersed between observations for the "wide field" survey in two separate ways. First, when the real-time analysis of recent images predicted a point spread function (PSF) above $1.1''$, the limit where weak lensing measurements can no longer be used for cosmology, the least recently observed supernova field that is visible will be observed. This first condition will not trigger supernova observations if all fields

Depth	Band	# Exps. x Exp. Time (s)	Total Exp. Time per visit (s)	5-σ limiting magnitude
Shallow	g	1 x 175	175	23.7
Shallow	r	1 x 150	150	23.6
Shallow	i	1 x 200	200	23.5
Shallow	z	2 x 200	400	23.3
Deep	g	3 x 200	600	24.6
Deep	r	3 x 400	1200	24.8
Deep	i	5 x 360	1800	24.7
Deep	z	11 x 330	3630	24.4

Table 2.2: Exposure times for DES-SN shallow fields and deep fields by band per visit, broken down by individual exposure length, and the fake SN-measured single visit 50% limiting magnitude depth.

have been observed in the last 4 days. Alternatively, any supernova fields which have not been observed in the last 7 days will be forced at the next possible opportunity (when not obscured by clouds and at airmass < 2.0). This ensures a high enough cadence to detect, classify, and measure cosmological distances for supernovae.

The DES SNe were discovered in the "real-time" difference imaging pipeline (DiffImg, (79)), where deep coadded template images were subtracted from each supernova survey image ("search" image). An example of a "search" image, template image, and their difference produced by the DiffImg pipeline is in Figure 2.5. Then the subtracted images were scanned by Source Extractor (85) to find new sources that had appeared in between the template image and the survey image. Those SN candidates are then pared down to eliminate subtraction artifacts by human scanners in Y1 and Y2, and eventually by an autoscanner (Goldstein et al. 2015, (86)) to produce a set of real variable objects including supernovae, AGNs, variable stars, asteroids, and KBOs.

The recovery efficiency of that pipeline was tested throughout the duration of the survey by the insertion of fake SNe Ia into the pipeline at a variety of simulated redshifts and other SN parameters. The fake SNe Ia light curves (LCs) were generated prior to the survey using a set of realistic SN parameters (color, stretch, redshift, and host galaxy separation), and as images were processed, the light curves were sampled at the real observation times and artificial point sources were inserted into the images using the pipeline's measured zeropoint

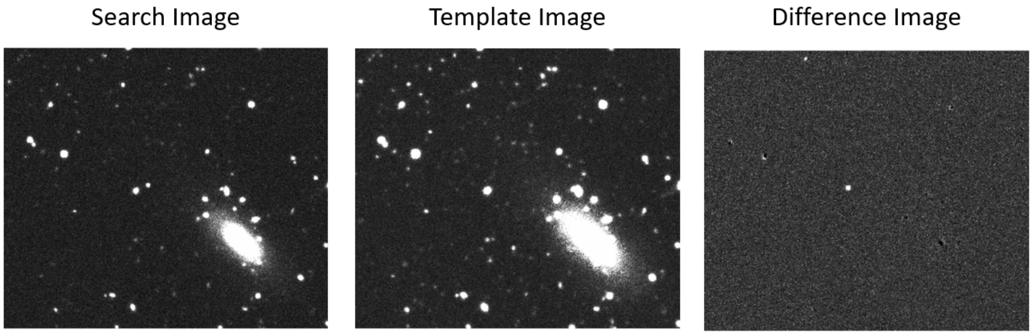

Figure 2.5: On the left is the search image from DES-SN field C3 in r band taken on September 11, 2014 during Y2 of DES-SN. The center image is an image from Y1 of the survey which does not have any supernova light in it. The image on the right is the result of running the image through the DiffImg pipeline which subtracts the template image from the search image. The dot in the center is SN DES14C3aod, a probable SN Ia with zPHOT = 0.24

and PSF, for a total of around 127,000 fake SNe Ia. Then the images were reprocessed with the inserted fakes.

The fake insertion algorithm took care to not overlay fakes on galaxies with active transients; however, if a fake SN was overlaid on a galaxy before a real supernova exploded, the real event would not be detected. For this reason, the number of host galaxies which were used for fakes was kept below 1% of catalog galaxies for most redshift bins, only deviating below z = 0.3 and above z = 1.1 since there were fewer galaxies to choose from at those redshifts, due to volume at low redshift and incompleteness at high redshift. See Figure 2 from Kessler et al. 2015 (79) for the distribution of fraction of galaxies with fakes with redshift.

As in other surveys, these fakes were used to model detection efficiency and survey depth. However, DES fakes made major improvements such as modeling the ideal detection efficiency as a function of Signal to Noise Ratio (SNR) enabling the use of fast Monte Carlo (MC) simulations to generate large numbers of light curves that are similar to those produced by DiffImg.

Over the course of the five year supernova survey, DES discovered over 30,000 events that it has considered for photometric typing in science analyses including both this analysis and the final photometric cosmology analysis. Of those events, the sample that passes our quality cuts (§2.5) totals 2077 events and is 3.0x as large as the sample used in the Perrett et al. 2012 (3) rate analysis from SNLS.

2.2 Photometry

Although the DES3YR analysis used the Scene Modeling Photometry (SMP) pipeline (87), this analysis will use the photometry from the DiffImg pipeline which was used to discover the SNe. This is due to the SMP photometry not yet being available for the entire sample. While the DiffImg photometry has 4x as many 5-σ outliers as the SMP photometry (0.08% vs 0.02%, compare $\sim$ 0.001% for a gaussian) and has slightly larger errors than the SMP photometry, it is much faster and is sufficient for the purposes of discovery, classification, and photometric redshift determination, which is all that is necessary for the rate analysis.

The photometric errors on the difference imaging were originally calculated from Source Extractor outputs (85), but due to various factors including host galaxy subtraction errors, the photometric errors as measured by Source Extractor tend to be underestimated. Therefore, DES-SN used the aforementioned fake SNe Ia with their known fluxes to calculate a map to adjust the photometric errors of the data to match those of the fakes as a part of the DES-3YR cosmology analysis (Brout et al. 2019 §4, (87)) [3]. Similarly, a map is constructed to adjust the scatter in simulations (see §4 for more information about simulations) to the scatter from fakes. The maps are tested by comparing the distribution of fit data parameters such as the FITPROB (probability of getting a χ^2 at least as large as the best fit χ^2 for that light curve, see §2.3 for information on light curve fitting) and the peak signal to noise ratio epoch (SNRMAX) between data and sim. Figure 2.6 shows the distribution of FITPROB (top) and SNRMAX (bottom) in sim (orange lines) and data (blue dots). The reduced χ^2 for the agreement between sim and data is shown in the legend as is the median value of

---

[3] Sam Hinton and Rick Kessler have created a new error correction map for the full 5 year data sample. DES-SN Internal communication

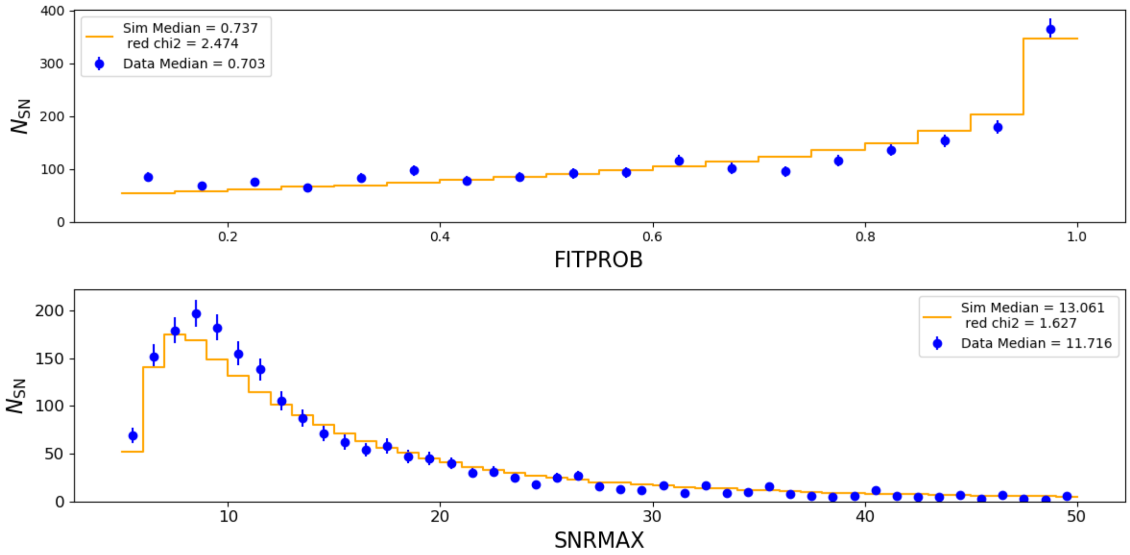

Figure 2.6: Distribution of fit probability for the SALT2 model (FITPROB) and maximum signal to noise ratio (SNRMAX) in sim (orange lines) and real data (blue dots) with nominal flux error correction.

each parameter in the sim and data. For comparison, the same distributions before error correction was applied are shown in figure 2.7. The error correction map creates a marked improvement in sim-data agreement.

2.3 Light Curve Fitting

Although SNe Ia are, without additional correction, relatively standard candles, it has been found that further standardization can make them even better distance indicators. First Phillips 1993 (12) found that the peak luminosity is higher for SNe Ia with slower decline rate (then parameterized as Δm_{15}, the decline in SN magnitude 15 days after peak). Second, Tripp 1998 (16) found that after standardizing supernova peak magnitudes based on decline rate, there was a remaining residual proportional to B-V color which, to the measurement precision he had at the time, made them perfectly standardized.

These relationships were combined into the Spectral Adaptive Lightcurve Template (SALT) for SNe Ia by Guy et al. 2005 (88), a model based on the Nugent et al. 2002 (89) template spectrum. That model was then trained on photometric data, allowing the template spec-

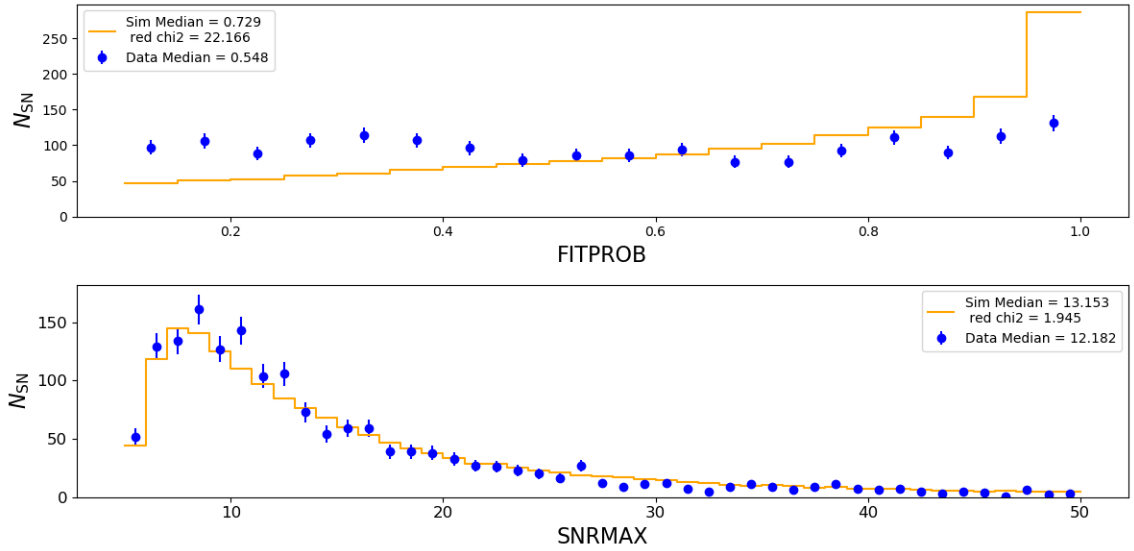

Figure 2.7: Distribution of fit probability for the SALT2 model (FITPROB) and maximum signal to noise ratio (SNRMAX) in sim (orange lines) and data (blue dots). Simulation as well as light curve fitting of data were done without flux error correction.

trum to vary with color, decline rate, and luminosity to match the data.

Then a similar model was trained on spectrophotometric data by Guy et al. 2007 to create SALT2, whose basic model parameterization we still use today. This model parameterized light curve shape using the x1 (stretch) parameter, color as the c parameter (estimated B-V color at peak), and peak luminosity as a prefactor x_0. Typical SN Ia color values are $|c| < 0.3$ and typical SN Ia stretch values are $|x1| < 3.0$, and the parameters are chosen such that the typical median values for SNe Ia are zero for both parameters. The form of the model spectrum is shown below in equation 2.1:

$$F(c, x_0, x_1, p, \lambda) = x_0 \times [M_0(p, \lambda) + x_1 M_1(p, \lambda)] \times exp[c\, CL(\lambda)] \tag{2.1}$$

The model predicts a spectrum, F, as a function of supernova parameters (c, x_0, x_1), a mean SN Ia spectrum (M_0), the component of the SN spectrum variability due to stretch (M_1), the average color law (CL), number of rest frame days pre/post peak (phase, p), and wavelength (λ). This model is used to fit light curves by minimizing the χ^2 between the observed broadband magnitudes and the magnitudes obtained by redshifting the model spectrum and multiplying it by the combined atmospheric, telescope, and instrumental transmission function. For a light curve fit with this method, the distance modulus μ, a logarithmic measure of luminosity distance, is given by the Tripp Estimator in Equation 2.2 below:

$$\mu = M_0 + m_B + \alpha x_1 - \beta c, \tag{2.2}$$

α and β are global fit standardization parameters which correspond to the Phillips “broader-brighter” relation and the Tripp “bluer-brighter” relation respectively, $m_B = -2.5\log_{10}(x_0)$, and M_0, unlike in equation 2.1, is the mean SN Ia absolute magnitude, also a global fit parameter.

The SNANA software package provides the code to fit the light curves using this model. We use the most recently trained SALT2 model that was developed for the Joint Light-curve Analysis (JLA, Betoule et al. 2014, Mosher et al. 2014 (90; 91)) and extended into the rest frame UV and IR by Hounsell et al. 2018 (92).

The light curve fitting is performed by first finding the time of peak flux using the ’Fmax-clump’ method combined with a fit to the Bazin function (93) shown below in equation 2.3:

$$A\frac{e^{-\frac{t-t_0}{\tau_{\text{fall}}}}}{1+e^{-\frac{t-t_0}{\tau_{\text{rise}}}}} + B \tag{2.3}$$

where t_0 is the epoch of peak flux, τ_{rise} and τ_{fall} are the rising and falling timescales respectively, and A and B are constants. This method takes the highest flux epoch within the densest clump of high SNR epochs as the initial estimate of the peak epoch and then using that as the initial guess for the fit to the Bazin function.

After the peak date has been fit, then the light curve is fit using the χ^2 minimizer, MINUIT (94). This fit is done in multiple iterations, with the first iteration having an additional error added (3% of max flux) to prevent MINUIT from finding false/local minima. An additional step that is taken when using SN-only photometric redshift fitting (see §2.3.1) is a small Monte Carlo Markov Chain (MCMC) burn in to account for the increased likelihood that MINUIT will find a local minimum when fitting for redshift along with the other LC fit parameters.

In addition to the standard χ^2 statistic, the SALT2 model includes additional covariance terms. One term is a penalty if the best fit milky way reddening coefficient is not the same during all epochs and the other is an additional penalty for the broad-band colors (e.g. $g-r$, $r-i$, $i-z$) varying differently than the model predicts beyond the penalty for the data not fitting each individual band's model.

That total χ^2 with covariances is then converted to the probability to exceed for the number of degrees of freedom. That value is known as the fit probability or FITPROB. This value would be uniformly distributed in the ideal case where errors are perfectly modeled.

Figures 2.8-2.11 show sample light curve fits (lines) to the photometric data points (dots) for several typical photometrically classified DES SNe Ia at a range of redshifts. At higher redshifts, the g band drops out of the fit because the flux is redshifted out of that band. The light curve fit parameters are displayed on the top of the plot.

2.3.1 Validation of Photometric Redshifts in Light Curve fitting

Unlike previous analyses with the DES-SN sample, which used redshift information from the SN or host spectra, we include a photometric redshift as an additional parameter in the light curve fit. This was originally done by Kessler et al. 2010 (73) on SDSS data and some publicly available SNLS data and by Palanque-Delabrouille et al. 2010 (95) using the SNLS data sample. We use the LCFIT+z method developed by Kessler et al. 2010 (73). They evaluate their method's accuracy using a metric they term Δ_z ($\Delta_z = \frac{z_{\text{phot}}-z_{\text{spec}}}{1+z_{\text{spec}}}$) which accounts for the expected increase in fit error at higher redshifts by adding a factor of $\frac{1}{1+z_{\text{Spec}}}$. When using the LCFIT+z method on the SDSS data with the original SALT2 spectral template, i.e. not the updated JLA + Hounsell et al. 2018 (90; 91; 92) model I use here, Kessler et al. 2010 (73) find $\sigma_{\Delta z}$ of 0.027. Figure 2.12 shows the distribution of

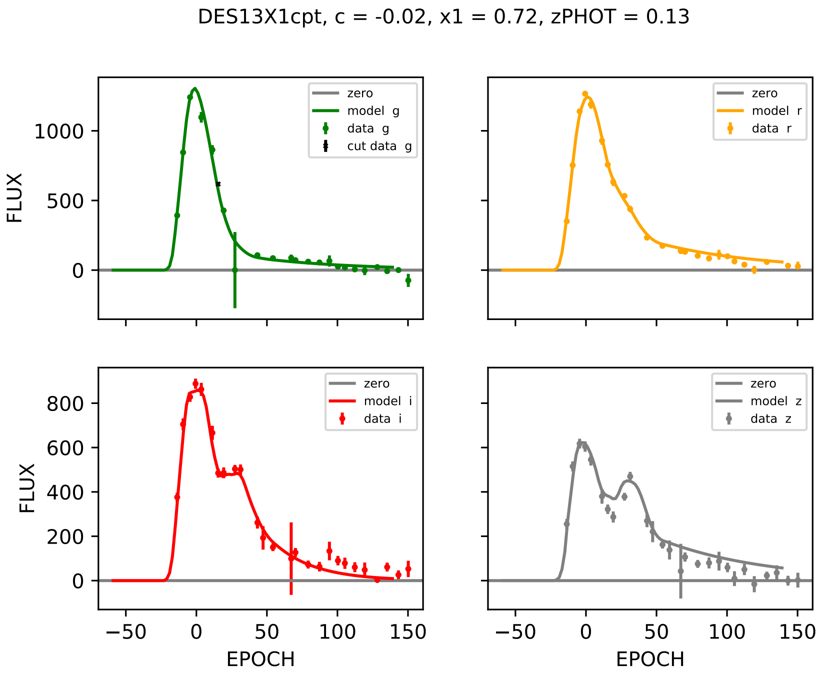

Figure 2.8: *griz* photometry (dots) and light curve fits (lines) to supernova DES13X1cpt. This is a typical photometrically classified SN Ia at redshift 0.133.

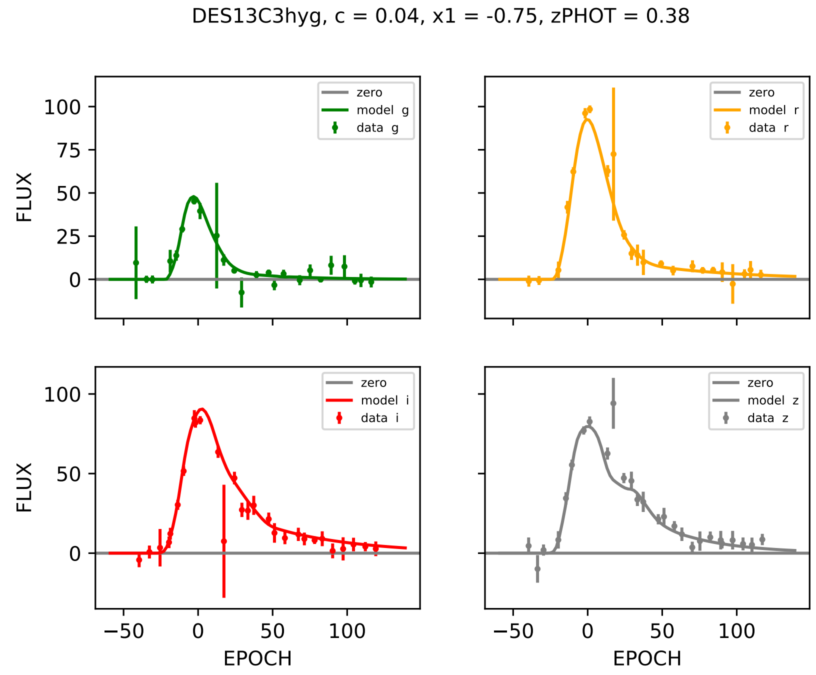

Figure 2.9: *griz* photometry (dots) and light curve fits (lines) to supernova DES13C3hyg. This is a typical photometrically classified SN Ia at redshift 0.318.

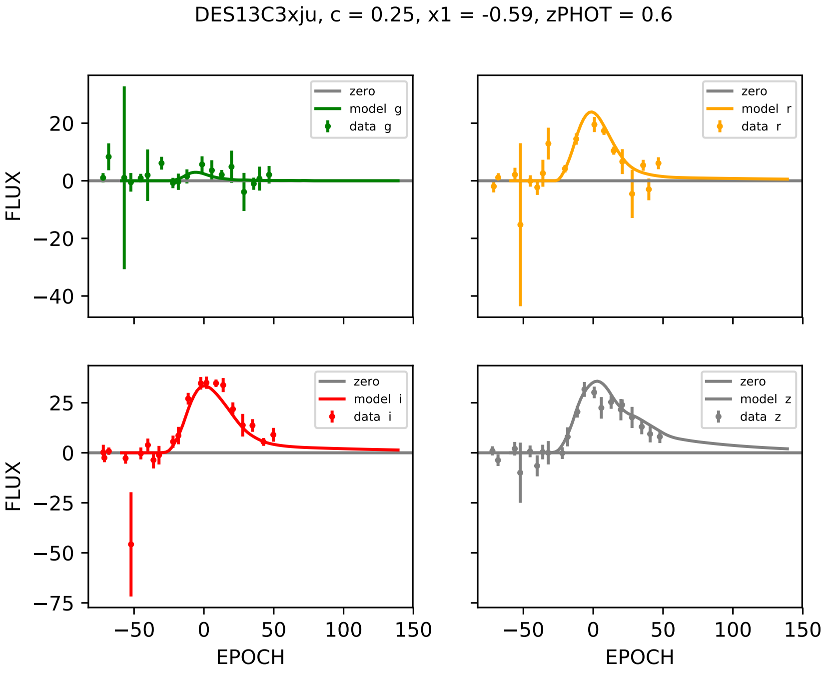

Figure 2.10: *riz* photometry (dots) and light curve fits (lines) to supernova DES13C3xju. This is a typical photometrically classified SN Ia at redshift 0.605.

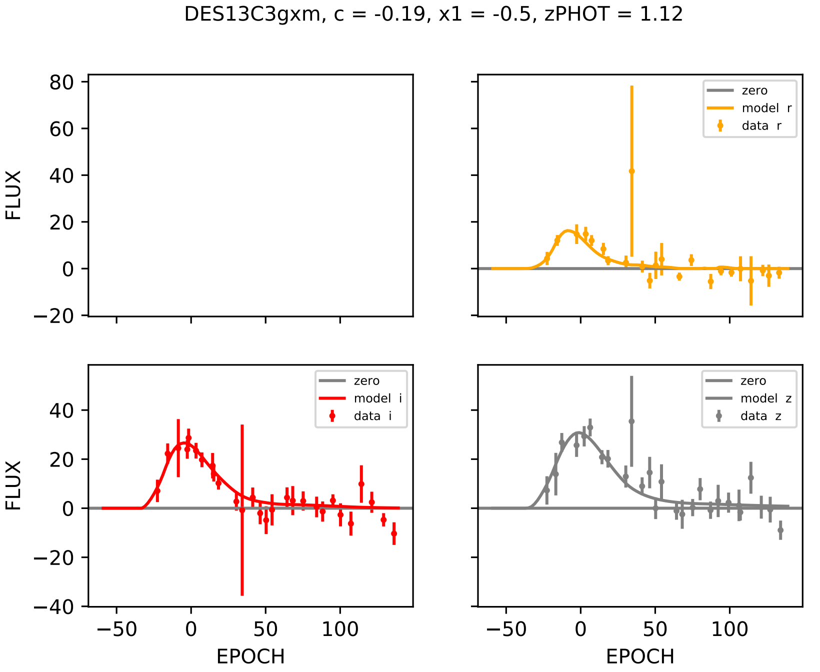

Figure 2.11: *riz* photometry (dots) and light curve fits (lines) to supernova DES13C3gxm. This is a typical photometrically classified SN Ia at redshift 1.122.

the difference between host galaxy spec-z, for the 1335 DES-SN host galaxies where that information is available, and their fit photo-z along with the same distribution for a subset of simulated SNe which pass a model of the spectroscopic selection cuts. The data and simulated events also pass all of the sample definition cuts outlined in §2.5. While the data outliers in that figure are visually striking, the most extreme outlier bins only contain one single data event and for the vast majority of the bins, the agreement between simulation and data is better.

Figure 2.13 shows the same distribution in Figure 2.12, after removing events that are 3-σ outliers relative to the photometric redshift fit error. After removal of the 314 events (23.5%) that are 3-σ outliers, the summary statistics of mean and $\sigma_{\Delta z}$ agree well and the agreement of the shape of the distribution improves significantly. This shows that there is no mean bias due to the photometric redshift fit with an $\sigma_{\Delta_z} = 0.036$. Other than having a slightly lower median redshift (0.50 for the spectroscopic redshift sample, 0.55 for the entire sample) the sample of supernovae with host galaxy redshifts is a representative sample of the entire data sample, so we believe validation on this subsample is justified.

This also shows that the distribution of Δ_z is distinctly non-gaussian, having 23.5% 3-σ outliers in the data compared to 0.3% in the ideal gaussian. However for the simulation there are 20.3% 3-σ outliers, which shows that the Δ_z shape is similar in both the quasi-gaussian core and non-gaussian tails for both simulation and data.

2.4 Photometric Classification

Due to limited spectroscopic resources, we did not obtain spectroscopic confirmation for all probable SNe Ia. Overall 356 SNe Ia were spectroscopically confirmed with an additional 59 designated as SN-Ia?, a designation meaning that the classification is “highly probable but with some (well defined) uncertainty” (Smith et al. 2020 (84)). Using the Smith et al. 2020 definition of photometric SNe Ia, there are roughly 4500 SNe Ia which could have been targeted for spectroscopic followup, giving a spectroscopic confirmation rate of 9% overall.

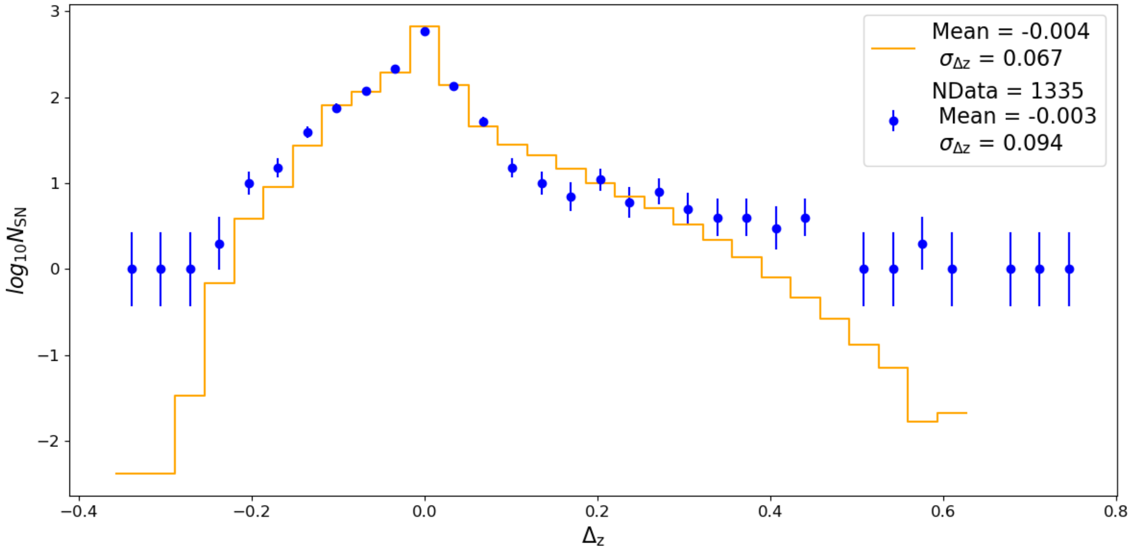

Figure 2.12: The distribution of the difference between spectroscopic host redshift and photometric supernova redshift for the subsample of 1335 DES Supernovae with host spectroscopic redshifts (blue dots) and the subsample of the simulation which pass selection cuts (orange lines).

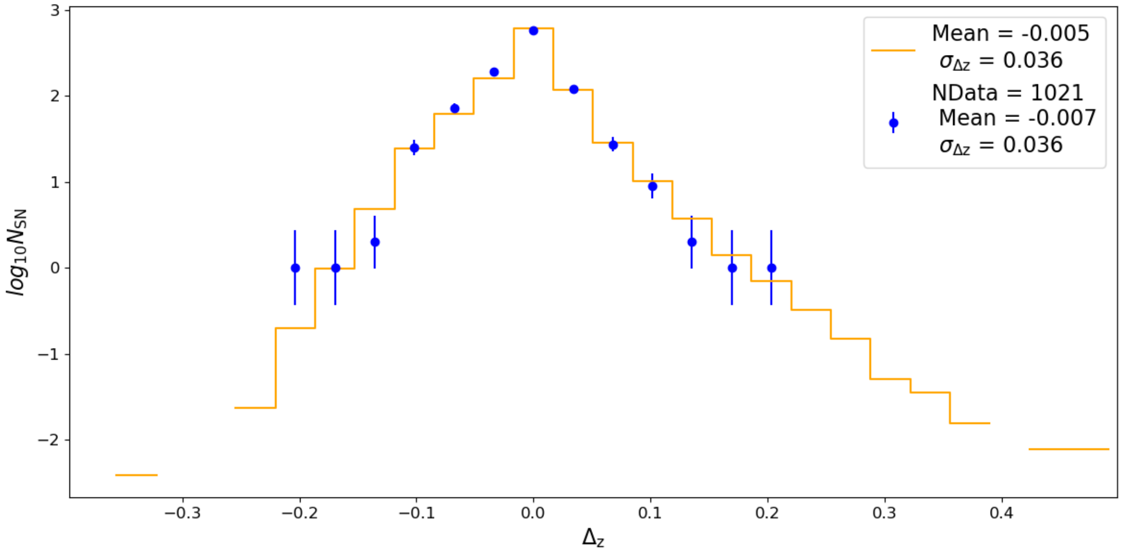

Figure 2.13: Same as figure 2.12, but after 3-σ clipping

In order to utilize the remaining 90% of the potential sample, we must use the multi-band light curves of the SN Ia candidates to photometrically classify them. The first method we used is cutting based on the probability to get a χ^2 to get a light curve fit to the SALT2 model as high as the best fit χ^2 (FITPROB). This cut removes more Core Collapse (CC) supernovae than SNe Ia since the FITPROB quantifies how well the light curve is described by the SALT2 spectral template which is based on data from SNe Ia.

Additionally, we used the "Radius Nearest Neighbor" (RNN) classification algorithm built into the SuperNova ANAlysis (SNANA[4], (96; 97)) software package. This algorithm uses a training set of simulated SNe Ia (see §4 for information about how supernovae are simulated), and a range of simulated contaminant supernova spectral models (SNIbc, SNII, peculiar SNe Ia) whose light curves are all fit as described in §2.3. Then, the events are divided into a 3-dimensional space by their fit color, stretch, and photometric redshift, since true SNe Ia tend to cluster in that parameter space. Then, using a test sample from the same model, the classifier quantifies how tight that clustering is in terms of an optimal radius for each dimension of parameter space. It does this by determining what distance of "neighbor" simultaneously optimizes SN Ia sample purity (% of sample which are true SNe Ia) and completeness (% of true SNe Ia which are classified as SNe Ia). It uses a statistic it calls "Figure of Merit" (FoM) which is equal to purity times completeness.

The classification is performed by taking each real event in parameter space, taking all simulated neighbors from the training set within all 3 radii of color, stretch, and redshift, and having them "vote" based on their true type. The probability of being an SN Ia is equal to the fraction of neighbors whose true simulated types are SNe Ia. In order to assign a type, whether it is an SN Ia or if it is any one of the types of contaminants (Type II, Type Ibc, or peculiarSN Ia), the classifier must have $1 - \sigma$ over 50% of neighbors be true SNe Ia. This means that if 3 of 4 neighbors are SNe Ia it will not assign a type ($\frac{3/4-0.5}{\frac{\sqrt{3}}{4}} = 0.6\sigma$) , but if 30 out of 40 are, it will assign type Ia ($\frac{30/40-0.5}{\frac{\sqrt{30}}{40}} = 1.8\sigma$).

---

[4] snana.uchicago.edu for manual and other information

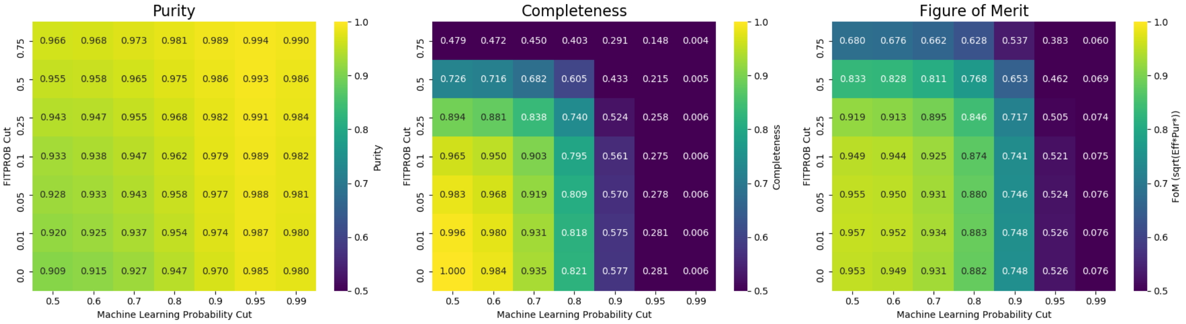

Figure 2.14: Heatmap showing the purity (left), efficiency (center), and figure of merit ($\sqrt{\text{purity} \times \text{efficiency}}$, right) of a simulated DES-like sample for several combinations of Radius Nearest Neighbor Classifier probability cuts (x-axis), and FITPROB cuts (y-axis).

Figure 2.14 shows the purity (left), completeness (center), and Figure of Merit (FoM, plotted as the square root of the figure of merit defined above ($\sqrt{\text{purity} \times \text{completeness}}$) so it is on the same scale as purity and completeness, right) of a simulated DES-like sample for several combinations of FITPROB and RNN probability cuts. Initially, the FITPROB and RNN probability cuts were selected based on highest FoM (FITPROB > 0.01 and RNN prob > 0.5 plus the 1-σ requirement), but after exploring the effect of choosing different cuts on the rate fit, we found that increasing the FITPROB cut to 0.1 produced a much lower χ^2 value for the power law rate fit than the original cuts, so we choose that cut for our nominal analysis

2.5 Defining the sample

Over the five years of the DES-SN survey, every object detected by the DiffImg pipeline on 2 separate nights that were determined to be real detections by the autoscan code(86) was catalogued. The DiffImg photometry from each event's coordinates for the full 5 year survey was stored. Those 31636 transient candidate light curves are the base of the sample.

From that point, the light curves for each candidate event are fit as described in §2.3. During this stage, many quality cuts are applied as in the DES3YR analysis (98). Cuts made to ensure good sampling of the light curve include requiring 5 observation epochs between 50 days before peak flux and 100 days after peak flux. Additionally, one of those epochs must be between 50 days before peak and the day of peak flux, and another epoch must be between 10 and 200 days after peak flux. A Signal to Noise Ratio (SNR) of at least 5 is required in 2 separate bands to ensure the light curve is well measured. Finally, we cut events with $|x1| > 3.0$ and $|c| > 0.3$ since normal SNe Ia do not have such extreme values of those parameters. Fast declining peculiar SNe Ia may have extreme events which fall outside of that range, but we do not include those in our analysis. These cuts in combination cause the largest reduction of candidate events from 31636 to 3747 (88% loss). 4% of all events were cut due to the sampling requirements, 40% were cut due to the SNR requirement, and the remaining 44% were cut due to the fit parameter cuts. Most events lost here are either not real SNe, too faint to be measured properly, or non-Ia transients. Out of the spectroscopically confirmed subset of 356 SNe Ia, 345 pass the sampling cuts (97.1%) and 311 pass the fit parameter cuts (87.3%). The relatively large number of spectroscopically confirmed SNe Ia that fail the fit parameter cuts are mostly highly reddened ($c > 0.3$) SNe Ia.

The next sets of cuts are designed to cut out remaining non-Ia transients while maintaining a mostly complete set of the observed SNe Ia. First is a cut on the light curve FITPROB, a measure of the goodness of fit for the light curve. A relatively tight cut of 0.1 (10% fit probability), 10 times stronger than the 1% cut used in the DES3YR analysis was motivated by an increase in the χ^2 for the rate fit. This cut removed around 700 events (18.9%) including 49 (15.8%) of the 311 remaining spectroscopically confirmed SNe Ia. Second, I apply the RNN classifier described in §2.4 and cut all events which are not successfully typed as SNe Ia. This includes events which are typed as CC as well as events for which SN Ia was the most likely type but the probability was not sufficiently high to assign a type. This cut removed 334 events (11.0%) including 18 (3.1%) of the 262 remaining spectroscopically confirmed SNe Ia.

The next cut is motivated by Fig. 2.15 and 2.16, which shows that events with higher Hubble residuals (distance modulus residuals to the reference cosmology, calculated using

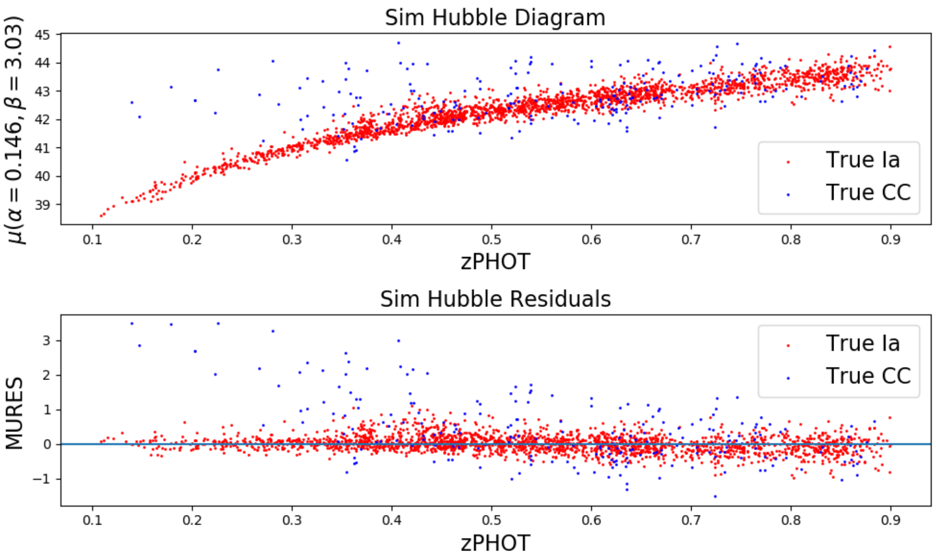

Figure 2.15: Hubble Diagram (μ vs. redshift) and residual to Hubble diagram fit (MURES) vs redshift for a DES-like simulation. True SNe Ia are red and true core collapse SNe are blue.

the Tripp Estimator, Eq. 2.2, and the α and β standardization parameters taken from the DES-3YR cosmology analysis) are dominated by CC supernovae. In order to not cut out events for which Hubble residuals may be large but uncertain, I cut out all events where the Hubble residual is greater than twice its error. This cut removed 340 events (12.6%) including 18 (7.4%) of the 244 remaining spectroscopically confirmed SNe Ia.

Finally, the sample is cut down to a redshift range where we have good statistics and where we would expect a good fit to our power law rate model. A combination of analyzing the number of events in each redshift bin, the trend in ratio between data and sim events with redshift (Figure 2.17), the potential turnover in rate power law at or near $z = 1.0$, and the χ^2 of the rate fit led me to choose a redshift range of 0.1 to 0.9. The effect of changing the redshift range is examined as a systematic in §5.2. This final redshift cut removed 284 events (12.0%) but no spectroscopically confirmed SNe Ia, leaving a final analysis sample of 2077 Supernovae. The effect of this redshift range cut on the rate fit is discussed in §5.2.

These cuts are designed to maximize purity of the sample while maintaining a completeness where the statistical error does not outweigh our systematic errors. The impact of these

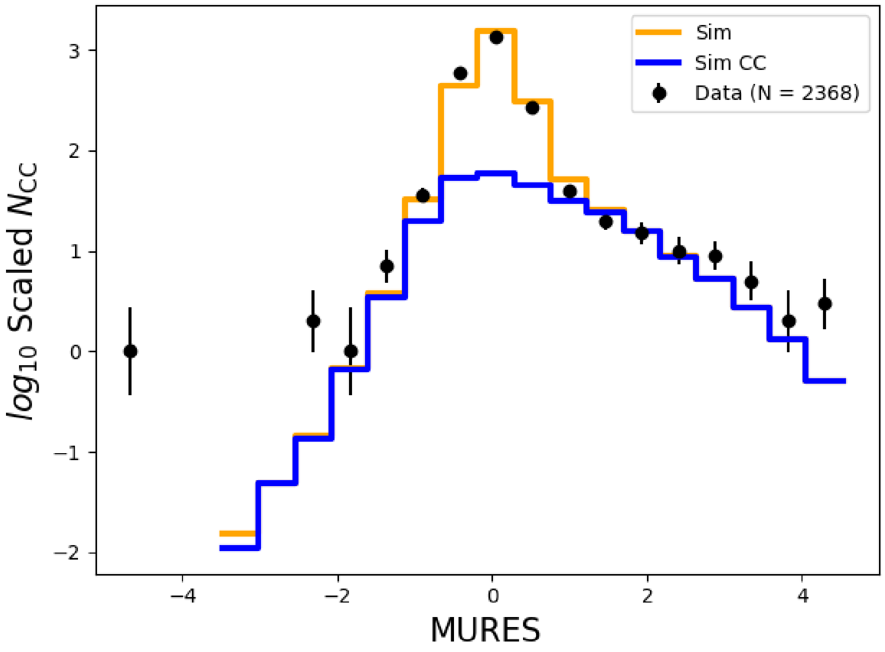

Figure 2.16: Distribution of Hubble diagram residual (MURES) for the nominal DES-SN sample (dots) and a DES-like simulation (lines). The total simulated SN distribution is in orange and the subdistribution of true core collapse SNe is blue.

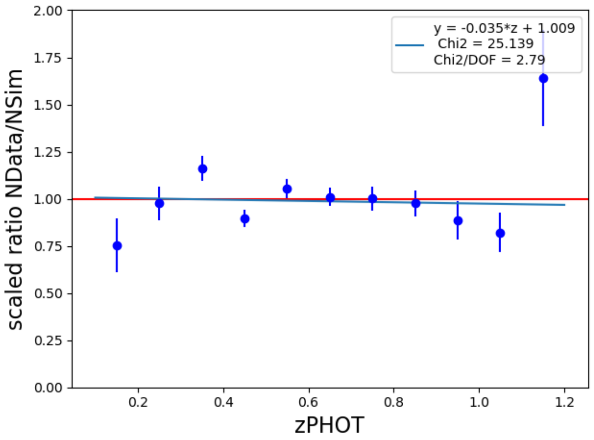

Figure 2.17: Ratio between data photometric redshift distribution and simulation photometric redshift distribution (blue dots). The best fit trend line to that ratio vs redshift is also in blue. The ideal ratio of 1:1 is shown as a red line for comparison. This figure shows the entire redshift range of the data. For the same figure showing only the redshift range used in the nominal analysis, see Figure 5.2.

Cut Level	Num. (%) events remaining	Num. (%) Spec Ias remaining
ML+2 detections	31636 (100)	356 (100)
LC Quality Cuts	3747 (11.8)	311 (87.3)
FITPROB > 0.1	3035 (9.59)	262 (73.6)
RNN Classified as SN Ia	2701 (8.53)	244 (68.5)
Hubble Residual $< 2\sigma$	2361 (7.46)	226 (63.4)
$0.1 < zPHOT < 0.9$	2077 (6.57)	226 (63.4)

Table 2.3: List of quality cuts applied to the sample and the number (%) of total events and spectroscopically confirmed SNe Ia that survive each level of cuts.

selection cuts is well modeled by our simulations (see §4) and we will demonstrate the impact of several of these choices in our systematic tests (see §5.2).

CHAPTER 3

FITTING THE SUPERNOVA RATE

I fit the SN Ia rate using a novel method based on the comparison of the data sample described above in Chapter 2 with the simulations described in chapter 4. In this chapter I present the χ^2 function that I minimize in order to fit the SN Ia in §3.1, I describe the modeling of the amount of core collapse supernovae in the sample by comparing the Hubble residual tails in the simulation and data in §3.1.1, and I describe the corrections made to the nominal DES-SN survey area to accurately model the volume observed by the survey in §3.2.

3.1 Explanation of the χ^2 function

Since SNe Ia are independent events with a slowly varying rate vs. redshift, the observed quantity of SNe Ia in each redshift bin should be Poisson distributed. Ordinarily, fitting Poisson distributed data to a model is done with maximum likelihood methods. Due to the central limit theorem, Poisson distributed events will eventually become well approximated by a Gaussian distribution with large enough sample size. In the redshift bin with the smallest number of events used in this analysis, there are 28 supernovae. The difference between the Poisson and Gaussian distributions with a mean of 28 peaks at 0.3% which is a much smaller deviation than any other uncertainty in the data or model. Therefore, we can use the Gaussian approximation to the Poisson distribution so the maximum likelihood method reduces to χ^2 minimization.

The χ^2 statistic is given by:

$$\chi^2 = \frac{(O_i - E_i)^2}{\sigma^2(E_i) + \sigma^2(S_i)}$$

(3.1)

where O_i is the observed number of events in a photometric redshift bin i and E_i is the "expected" or modeled number of events in that same photometric redshift bin. $\sigma(E_{,i})^2$ is the variance on the modeled number of events in the photometric redshift bin i and $\sigma(S_i)^2$ is the variance due to the finite size of the simulations used to construct the model.

For this analysis we use photometric redshift bins with $\Delta z = 0.1$ which is approximately equal to the photometric redshift uncertainty. We also choose the simulated redshift bin width to be the same as the photometric redshift bin width.

First we will define the "Observed" number of events. Since this is a photometric analysis we expect the number of events that we observe to include a non-zero number of core collapse supernovae in that sample. Therefore, we define our O_i as

$$O_i = N_{\mathrm{data,i}} \times \mathrm{Frac}_{\mathrm{Ia,i}} \tag{3.2}$$

The $N_{\mathrm{data,i}}$ are the number of observed events in a photometric redshift (photo-z) bin and $\mathrm{Frac}_{\mathrm{Ia,i}}$ is the modeled fraction of those events which are true SNe Ia. In order to predict the fraction of core collapse events in each redshift bin $(1 - \mathrm{Frac}_{\mathrm{Ia,i}})$, we utilize the simulations described below in §4.

The naive approach to determining the fraction of core collapse events would be to simply take the fraction of the simulated events that pass all of our light curve quality cuts (§2.3) in each bin that are core collapse as the "true" fraction in the data. However, that relies on the relative normalization of the core collapse and SN Ia rates being correct. We can improve on this by using the data to scale the number of core collapse events while still using the simulated SNe to determine the shape of the redshift distribution of core collapse events. This is described below in §3.1.1.

We also use the simulated supernovae to determine our E_i or our expected number of events.

$$E_i = \sum_{J=1}^{N} N_{\mathrm{GEN}}^{J} \epsilon_{i,J} f_J f_{\mathrm{norm}} \tag{3.3}$$

The expected number of events in a photometric redshift bin i is given by the sum over all true simulated redshift bins J of the number of simulated events N_{GEN}^{J} times the simulated efficiency that a generated event with true redshift in bin J ends up in photometric redshift bin i, $\epsilon_{i,J}$. f_{norm} is a correction factor to scale down the large simulation to be the same scale as the data by a factor of 1 over the number of simulated surveys, and f_J are the fit parameters that adjust the Monte Carlo (MC) simulation rate to the best fit rate. Figure 3.2 shows the $\epsilon_{i,J}$ matrix that was used in the nominal analysis. The MC simulation rate was originally set to be the Perrett et al. 2012 (3) rate from SNLS (Rate = 1.7 x $10^{-5}(1+z)^{2.11}$ SN/yr/Mpc^{-3})), but was later set to our best fit rate parameters in order to reduce any potential effects of being far from the χ^2 minimum at the start of the fit.

Since the $\epsilon_{i,J}$ is not intuitive, Figure 3.1 is included as a visual aid. The upper panel in that figure shows the distribution of simulated SN Ia photometric redshifts with an arbitrary bin (bin "i") highlighted in red. The events in that bin are then separated into their respective true redshift bins in the lower portion of that figure. The element of the $\epsilon_{i,J}$ matrix for the arbitrary row chosen is thus the height of each bar in the lower histogram divided by the number of events simulated in that true redshift bin.

Finally we must define the variance on the expected number of events in each bin and the variance due to the finite size of the simulation. For the expected events, we expect Poisson noise on the modeled number of events in each bin therefore:

$$\sigma_{E_i}^2 = \sum_{J=1}^{N} N_{\mathrm{GEN}}^{J} \epsilon_{i,J} f_J f_{\mathrm{norm}} \tag{3.4}$$

For the variance due to the finite size of the simulations, we also expect Poisson noise on the modeled number of events, but scaled down by the normalization factor f_{norm} and scaled

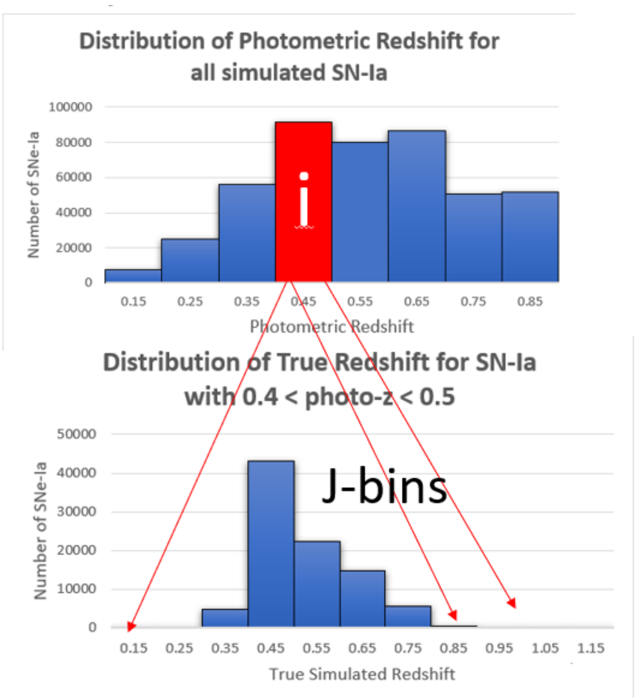

Figure 3.1: Visual representation of the $\epsilon_{i,J}$ matrix that is used in the χ^2 function. Shows that $\epsilon_{i,J}$ is the mapping of of how events in a photometric redshift bin i (upper panel) come from a range of true redshift bins (lower panel).

up or down by the fit factors f_J as shown below:

$$\sigma^2_{S_i} = \sum_{J=1}^{N} E_i f_J f_{\text{norm}} = \sum_{J=1}^{N} N^J_{\text{GEN}} \epsilon_{i,J} f_J^2 f_{\text{norm}}^2 \tag{3.5}$$

Therefore the entire χ^2 function that we minimize to determine the fit parameters f_J is:

$$\chi^2 = \sum_{i=1}^{N_{\text{bins}}} \frac{(n^i_{\text{data}} - \sum_{J=1}^{N} N^J_{\text{GEN}} \epsilon_{i,J} f_J f_{\text{norm}})^2}{\sum_{J=1}^{N} N^J_{\text{GEN}} \epsilon_{i,J} f_J f_{\text{norm}} (1 + f_J f_{\text{norm}})} \tag{3.6}$$

We minimize this χ^2 function using MINUIT (94), the same χ^2 minimizer used in the light curve fitting in §2.3.

In this analysis we do not fit the f_{J} values individually, but rather we fit a power law functional form of the f_{Js}

$$f_{\text{J}}(z) = \alpha \times (1 + z_{\text{J}})^{\beta} \tag{3.7}$$

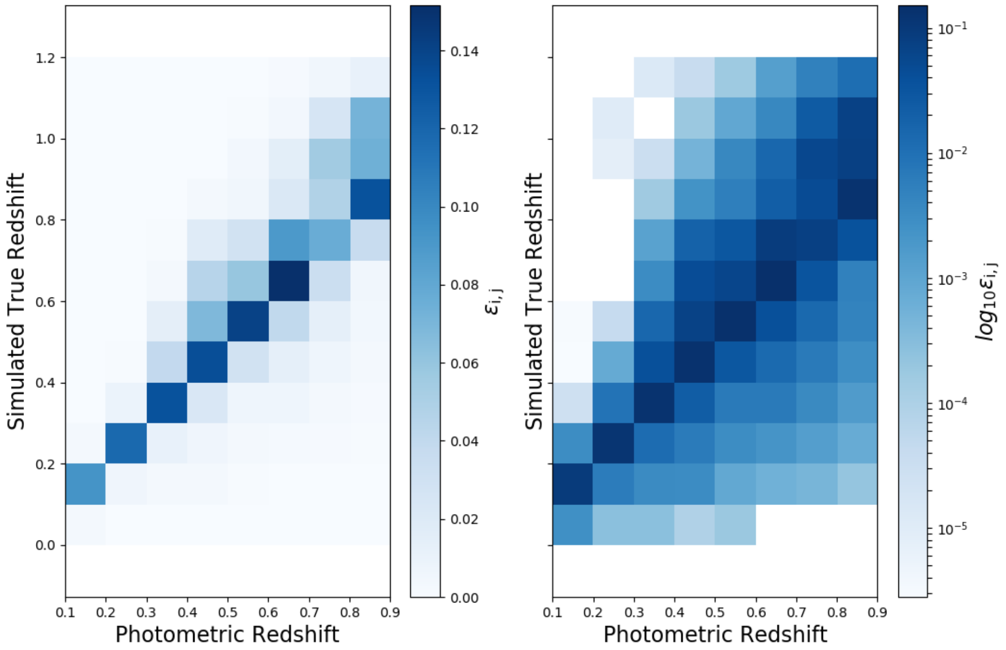

Figure 3.2: This plot shows the probability that a supernova that is simulated in the true redshift bin on the y-axis is both recovered and fit into a photometric redshift bin on the x axis. The scale (linear on left, logarithmic on right) is shown in the colorbar on the right hand side of each subplot. The axes are asymmetrical since we simulate out to the DES detection limit near z = 1.2 but only fit the SN Ia rate out to z = 0.9.

where α is the ratio between data and MC simulation power law normalizations, β is the difference between data and MC simulation power law indices, and z_{J} is the central redshift of simulated redshift bin J.

3.1.1 Core Collapse SN Scaling

Since the above model requires that I correct for the amount of estimated core collapse contamination in the photometric sample, I describe the more complex method (as compared to the naive method above) I use in the analysis.

In order to do this, I begin by considering only events whose measured distances for their measured redshift using DES3YR SN standardization parameters ($\alpha = 0.146; \beta = 3.03$) are substantially different than the redshift-distance relation in a standard ΛCDM model ($w = -1, H_0 = 70.0$km/s/Mpc). These events with high residuals to the Hubble diagram distance modulus (μ) fit or high Hubble residual (MURES) events for short, are more likely to be core collapse than SNe Ia because core collapse SNe tend to be several magnitudes fainter than SNe Ia. This can be visualized by looking at the simulation Hubble diagram residuals in Fig. 2.15 where true core collapse events are in blue and true Ias are in red. In order to maintain a high purity of core collapse events in the tails, we define the tails as $|\mathrm{MURES}| > 1.0$.

The scale factor is then calculated using this set of equations:

$$Norm \times (N_{\mathrm{Ia,sim}} + S \times N_{\mathrm{CC,sim}}) = N_{\mathrm{Tot,data}} \tag{3.8}$$

$$\begin{split} Norm \times (n_{\mathrm{Ia,sim}}(|MURES| > 1.0) + S \times n_{\mathrm{CC,sim}}(|MURES| > 1.0)) \\ = n_{\mathrm{Tot,data}}(|MURES| > 1.0) \end{split} \tag{3.9}$$

where $Norm$ is an overall normalization scaling the size of the sim to the size of the data,

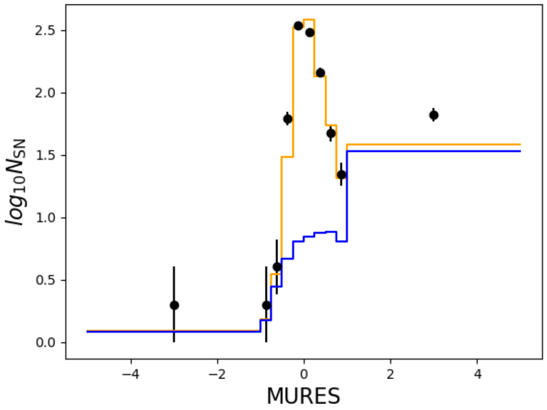

Figure 3.3: Distribution of Hubble Residual(MURES) for data (black dots), all simulated SNe (orange lines), and simulated CC supernovae (blue lines). There is only one bin of MURES beyond $|MURES| > 1$.

$N_{\rm Ia,sim}$ is the number of SNe Ia in the sim, $N_{\rm CC,sim}$ is the number of core collapse events in the sim, S is the relative scaling between the number of core collapse events in the sim and data. The lowercase "n" in the second equation refers to the same quantities as the capital "N" in the first equation except the numbers are only for the events in the Hubble Residual tail where |MURES| > 1.0.

Taking the ratio of Eq. 3.8 and Eq 3.9 and rearranging gives us this equation for the relative core collapse scale factor:

$$S = \frac{R \times N_{\rm Ia,sim} - n_{\rm Ia,sim}}{n_{\rm sim,CC} - R \times N_{\rm simCC}} \tag{3.10}$$

where:

$$R = \frac{n_{\rm Tot,data}}{N_{\rm Tot,data}} \tag{3.11}$$

The MURES distribution is shown for the low redshift scaling bin in Figure 3.3. The high MURES events are all grouped into a single high/low bin beyond $|MURES| > 1$ since that is how they are grouped in the scaling procedure. The core collapse scaling found for this bin in the analysis is 1.94, which is consistent with this visual.

3.2 True Field of View

Another ingredient in the rate fit is the implicit volume calculation in comparing our observed number of supernovae to the number of supernovae simulated using an estimated area calculation. In this section, I describe how I correct the nominal field of view (FOV) for DECam to the effective FOV that is capable of discovering and monitoring supernovae.

The previously referenced FOV for DECam of $\sim$2.7 deg^2, which totals 27.753 deg^2 over the 10 supernova fields, was determined for an ideal survey by taking the median area of a pixel (0.263” x 0.263”) and multiplying by the total number of pixels in a field ($\sim$ 500 Million). However, multiple sources cause the actual effective area to be reduced from this designed value. The estimated size of the area loss due to these sources is provided in table 3.1. These sources include:

1. Dead CCDs

   CCDs 2 and 61 were entirely dead for most/all of the survey.

   Half of CCD 31 died during the survey and all data from it was excluded due to a lack of template data.

2. CCD Border

   See Fig. 3.4 and Fig. 3.5 for the number of detections vs X and Y pixel coordinate near all CCD edges.

   The number of detections drops to roughly 50% at 25 pixels from the CCD edge in both X and Y, so we choose that as the effective CCD border. This is due to a combination of multiple effects dominated by image subtraction edge effects.

   The threshold to determine a “detection” was whether or not it was flagged as useful in the LC fitting. In addition, detections were only counted for events which passed the DES-3YR LC quality cuts with a weaker cut on fit probability (FITPROB > 0.001).

3. Masked Pixels

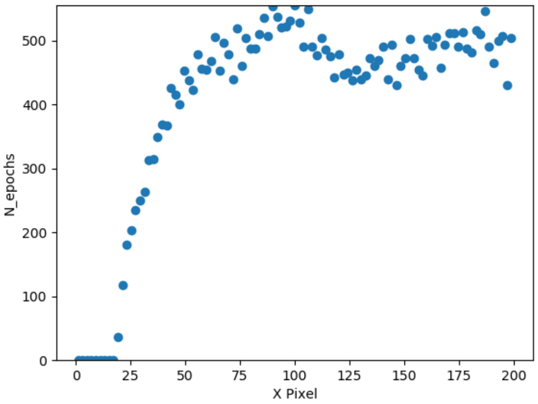

Figure 3.4: Number of observations of Fake SNe per X pixel coordinate.

During image processing, saturated pixels around bright stars are masked.

Number of masked pixels was taken from outputs of the DiffImg pipeline

4. Field Overlap

   The DES fields are divided into four groups, C (C1, C2, C3), E (E1, E2), S (S1, S2), and X (X1,X2, X3), and each group is tightly clustered on the sky. This clustering also leads to small overlaps

   The overlapping area was determined by looking at a simulated sample of SNe using the DES_DIFFIMG SIMLIB, which contains information about observations in multiple fields in a form of virtual Monte Carlo integration (see §4 for more information about the simulations and SIMLIB).

   The exact calculation of the overlapping area (A_{Overlap}) for a pair of fields with estimated area (A_{Tot}), total number of observed SNe ($N_{\mathrm{SN,tot}}$), and number of SNe in the overlapping area ($N_{\mathrm{SN,overlap}}$) is: $A_{\mathrm{Overlap}} = A_{\mathrm{Tot}} \times N_{\mathrm{SN,overlap}}/(N_{\mathrm{SN,tot}} + N_{\mathrm{SN,overlap}})$. The number of SNe in the overlapping area must be added back into the denominator to count the area from both overlapping fields.

This corrected area (Table 3.1) was fed back into the simulations to generate the number of expected supernovae for the desired number of DES seasons.

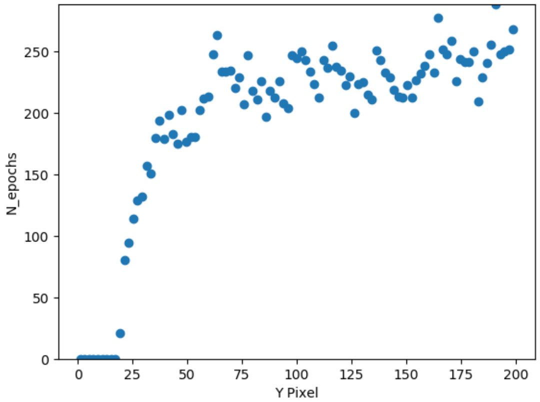

Figure 3.5: Number of observations of Fake SNe per Y pixel coordinate.

Source of Loss	Area Lost (deg^2)	Area (deg^2)	Fraction of Total Area
None	-	27.753	1.000
Dead CCDs	1.343	26.41	0.952
CCD Border	0.959	25.451	0.917
e Masked Pixels	1.575	23.876	0.860
Field Overlap	0.963	22.912	0.826

Table 3.1: Breakdown of the different sources of loss of effective area in the DES-SN survey. These include the dead CCDs (CCD 2, 31, and 61), a 25 pixel border region where the effective detection efficiency drops below 50% of its average value, pixels which are masked due to bright sources, and area that is double counted due to field overlap. Our designed area of 27.753 deg^2 (0.008454 ster) is reduced to an effective area of 22.912 deg^2 (0.006979 ster), a loss of 17.4%.

CHAPTER 4

SIMULATIONS

The method described in Chapter 3 requires a large number of simulated supernovae to determine the rate by comparison. It also requires the simulations to determine the estimated core collapse contamination that is removed from the rate fit. Simulated light curves can also be used to validate both the rate fitting method and light curve fitting methods. For these reasons, I describe the simulation method in §4.1, the simulation validation in §4.2, the correction of the simulation method for anomalous efficiency in §4.3, and the validation of the rate fit method in §4.4.

4.1 Simulation Methodology

The large number of simulated light curves required for this analysis are generated by the SuperNova ANAlysis (SNANA[1], (96), (97)) software package.

SNANA is a widely used suite of code which uses a combination of real observation data and model information to generate light curves with similar characteristics to those of supernova surveys. The real data includes host galaxy libraries (Gupta et al. 2016, (99)), a survey simulation library (SIMLIB), measured system transmission functions, and pipeline detection efficiency measured by fake SNe.

The host galaxy libraries include redshifts for galaxies in the survey footprint as well as other properties such as host surface brightness profiles, and stellar mass. The SIMLIB contains actual observation cadences and conditions (including PSFs, zeropoints, CCD gain, and sky brightness). The system transmission functions are used to calculate the simulated "true" magnitude for the simulated supernova SEDs. The pipeline detection efficiency gives a probability that the DiffImg pipeline will register each epoch as a detection based on the observed SN magnitude.

---

[1] snana.uchicago.edu for manual and other information

The model information includes the SN population models from Scolnic and Kessler 2016 (distributions of color and stretch (100)), the volumetric SN Ia rate from SNLS (Perrett et al. 2012 (3)), core collapse SN rate from Strolger et al. 2015 (101), SN Ia intrinsic scatter model from Guy et al. 2010 (102), SN Ia spectral models (SALT2; Guy et al. 2007, Betoule et al. 2014, Hounsell et al. 2018 (103; 90; 92)) and core collapse SN spectral models (Jones et al. 2017 (104)).

The SN Ia spectral models are the same SALT2 model described in §2.3. The core collapse SN models are a set of templates based on individual observed core collapse SN light curves and spectra which have been "mangled" (warped on a filter-by-filter basis) to match the light curves. The templates were then adjusted in luminosity and relative fraction to match the observed CC distribution.

SNANA generates simulated lightcurves using the above information in this manner.

1. Determine number of fake SN light curve to generate in redshift bins based on the volumetric rates and the survey sky coverage (solid angle)

2. For each light curve to be generated, select a redshift from the above distribution, a date of peak brightness (PKMJD) from an input range (the duration of the survey), host galaxy, and supernova parameters which are either color (c) and stretch (x1) from the input distributions for SNe Ia or a template LC for core collapse.

3. Take the template SED for the given SN at all observed epochs, and apply astrophysical effects such as redshift (including peculiar velocity randomly chosen from a gaussian) and Milky Way extinction.

4. For each of those "top of the atmosphere" spectra, apply the system throughput function to get a "true" magnitude in each filter for each epoch.

5. For every observation, use information in the SIMLIB (PSF, zeropoint, sky background, CCD gain, etc) to convert the "true" magnitude into a true observed flux.

6. Apply poisson noise to flux based on the above quantities to produce an "observed" flux.

7. Use detection efficiency measured by fake SNe to determine whether or not each epoch is detected

8. If event is counted as a detection in two bands on any two nights, then it is included as a candidate.

4.2 Simulation Validation

One of the challenges of simulating realistic supernova light curves is accounting for various unknown and/or unmodeled factors in the simulation. One well-known issue with this is the non-Poisson relationship between host surface brightness and flux scatter relative to the Poisson error first outlined in Kessler et al. 2015 (79). This issue and others necessitate the creation of a flux error map which depends on at least host surface brightness, but potentially other factors such as PSF size and initial SNR.

These flux error maps are created by taking the overlaid fake supernovae which were also used to monitor efficiency (see Kessler et al. 2015 (79)) and matching their known flux and flux error values with the values obtained by processing the images with the fake supernovae through the DiffImg pipeline. This procedure is done twice, once to match the simulated supernovae to the fake SNe and once to match the actual data to the fake SNe.

In order to test the agreement of the flux errors on the scale of entire light curves, we can compare fit parameters which are directly related to the flux errors, such as SNRMAX (highest signal to noise ratio epoch of the light curve) and FITPROB (probability of getting a χ^2 at least as large as the best fit χ^2 for that light curve). Comparisons between those parameters are shown in Figures 2.6 and 2.7 in section §2.3.

In addition to testing those parameters which directly depend on the flux errors, we can also test whether the simulation matches the data distribution of LC fit parameters in Figure

4.3 and the errors on those parameters in Figure 4.2.

This agreement between simulation and data is important for two reasons. First, it is a necessary prerequisite for all cosmological analyses using this data set that the simulations resemble the data. Second, the rate fitting method described in §3 implicitly requires the simulation to be nearly identical to the data in all respects except the redshift distribution/rate. The most important subdistribution to match for the nominal analysis is the photo-z smearing (zPHOT- zSPEC distribution, Figures 2.12 and 2.13) since that directly enters the χ^2 function as the transfer matrix/efficiency function. However, in order for this agreement to not be disrupted by the sample selection cuts, we must also match the distributions in the LC fit parameters (c, x1, mB) and the parameters that we cut on (FITPROB, SNRMAX, NN_PROB_Ia, and MURES).

4.3 Correcting Simulation for Anomalous Fake SN Efficiency

When inspecting an early version of the data, I noticed a several sigma discrepancy between the simulation and data in the lowest redshift bin ($0.1 < z < 0.2$) relative to the simulation. This persisted after adjusting for a linear trend in the ratio between sim and data events as a first order adjustment for the difference between the simulation SN rate and the data SN rate. At the same time, DES-SN discovered that a substantial amount of low redshift ($z < 0.3$) fake supernovae were successfully overlaid on images but were either not successfully detected or were detected only a few times with low scores from the autoscanner algorithm[2].

The aforementioned low redshift fake SNe are bright enough that they are certain to be detected on a generic patch of sky, which is what SNANA simulates. However, since they were not detected due to various factors (e.g. gaps between chips) the detection efficiency is artificially low. This means that we must correct for this effect in our simulations by lowering the simulation low redshift efficiency to match the fake efficiency.

Figure 4.4 shows the fraction of overlaid fake SNe that are detected. Overplotted on

---

[2] Rick Kessler, DES-SN internal communication

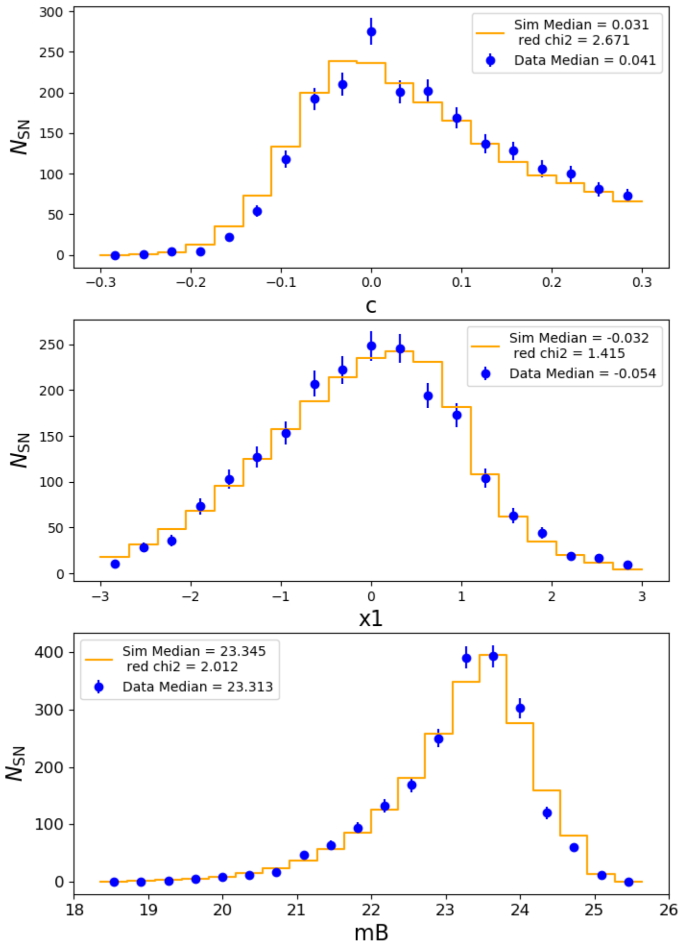

Figure 4.1: Distribution of light curve fit color (c, top), stretch (x1, middle), peak brightness (mB, bottom) in sim (orange lines) and data (blue dots).

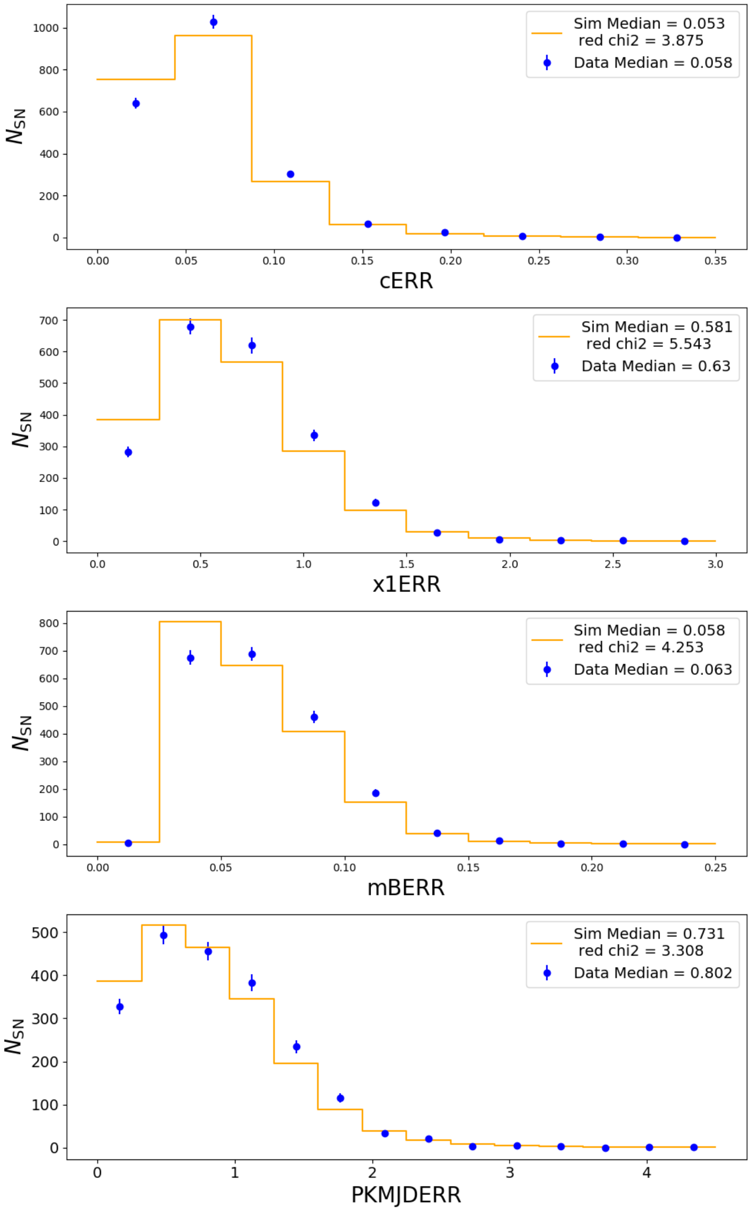

Figure 4.2: Distribution of the errors on light curve fit color (cERR, top), stretch (x1ERR, upper middle), peak brightness (mBERR, lower middle), and date of peak brightness (PKMJDERR, bottom) in sim (orange lines) and data (blue dots).

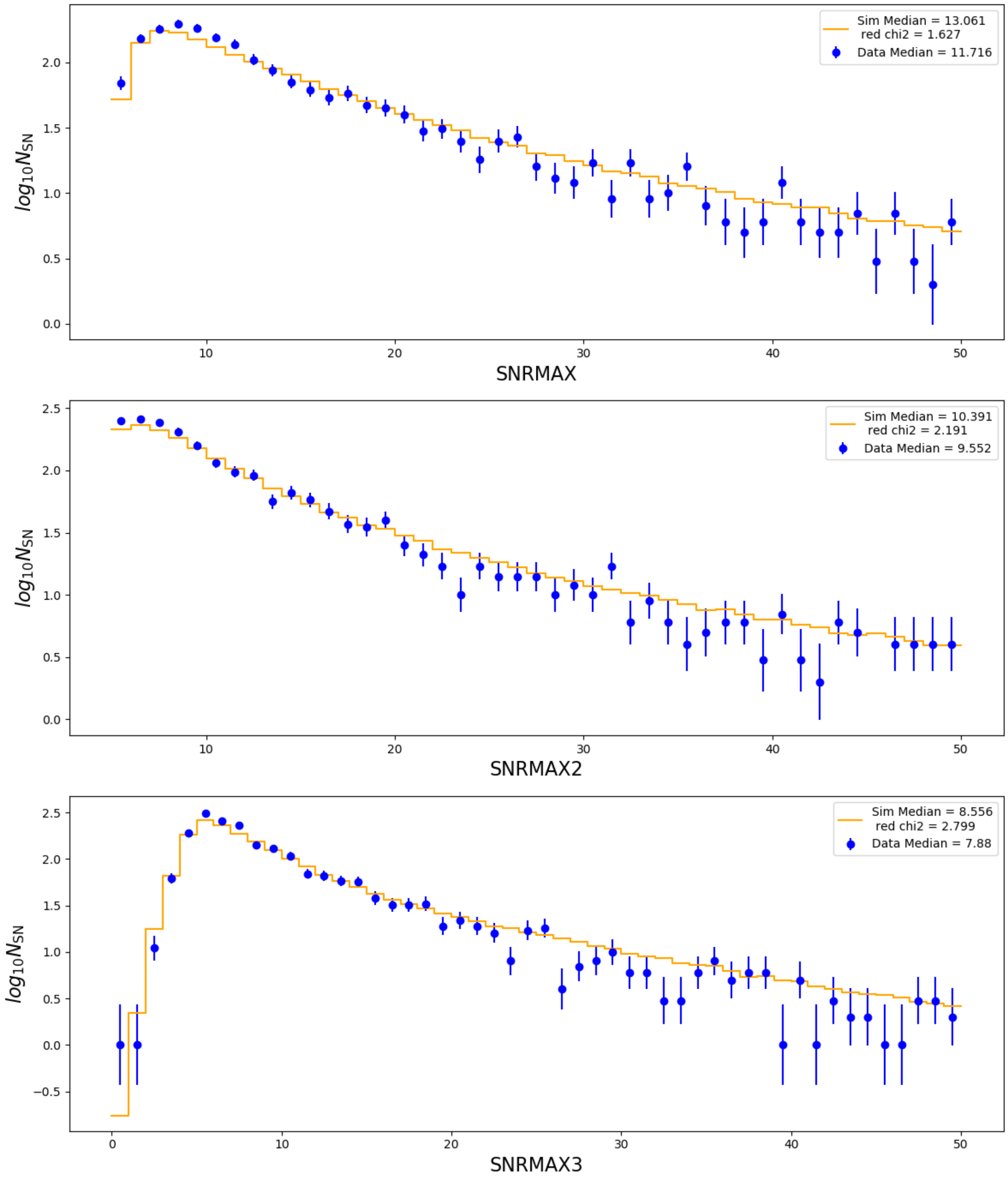

Figure 4.3: Distribution of SNR at the highest 3 SNR epochs (SNRMAX, SNRMAX2, and SNRMAX3) in sim (orange lines) and data (blue dots).

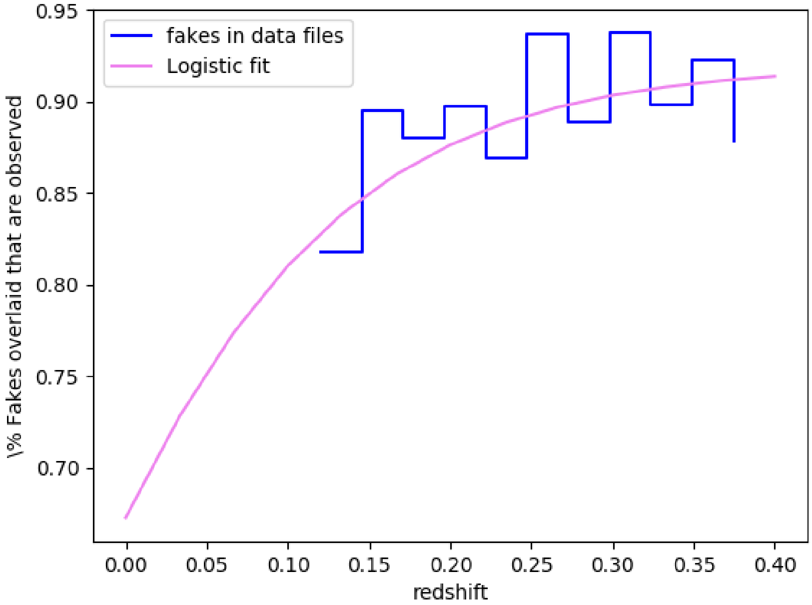

Figure 4.4: Percentage of overlaid fakes which passed DES trigger requirements and were recorded as "observed" vs. redshift. Overplotted is the logistic curve which we used to approximate this efficiency.

the distribution is the logistic function that we used to approximate this anomalous fake supernova efficiency. We extrapolated that function down to low-redshifts where we did not have fake supernova data and higher redshifts where we could not assume completeness. The results of using that function as an input efficiency map to our simulations is shown in the panels of Figure 4.5. This figure shows that the simulation is faithfully reproducing the efficiency map in the simulated true redshift distribution and is nearly exactly reproduced in the photometric redshift distribution.

4.4 Rate Method Validation

We test the validity of the formalism in §3 by using sets of 48 data-size simulations with different input rates. We run the data-sized simulations through the same pipeline as the data and check if we recover the known input rate. Figures 4.6 and 4.7 show that we can recover the input rate for power law β between 1.32 and 2.22, a large range around our best

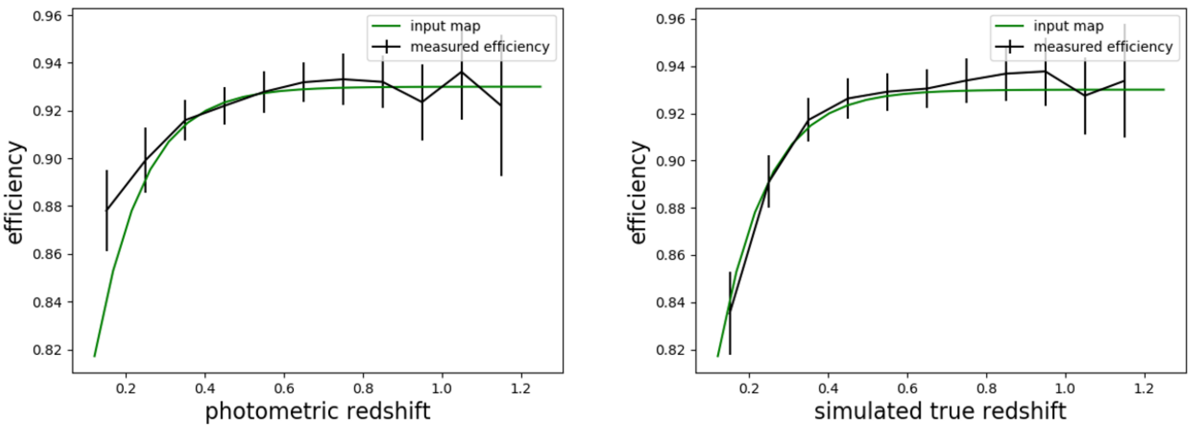

Figure 4.5: Percentage of simulated supernovae which pass simulated DES trigger requirements after the efficiency map shown in Figure 4.4 and overplotted again in green on this figure is applied. Percentage is plotted vs. photometric redshift (right) and simulated true redshift (left).

fit β and containing the Perrett et al. 2012 (3) rate which was the first MC comparison sim rate used. Since we don't test validation at larger differences of beta, we ultimately simulated a new comparison MC sample with our best fit rates in order to confirm there is no large shift.

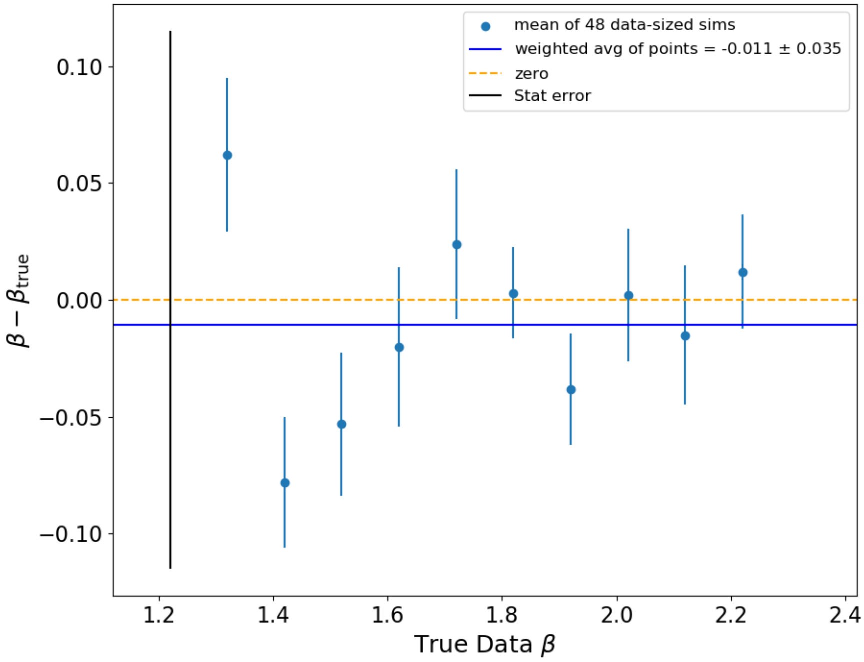

Figure 4.6: The x-axis shows the “true” β for the simulated data-sized samples on which the rate method is validated. The position on the y axis for each dot shows how different the mean of the fit β over the 48 data-sized simulated samples at each “true” β were from the true β in the simulation. All of these used a MC comparison sim with $\beta = 1.82$ as found in this work.

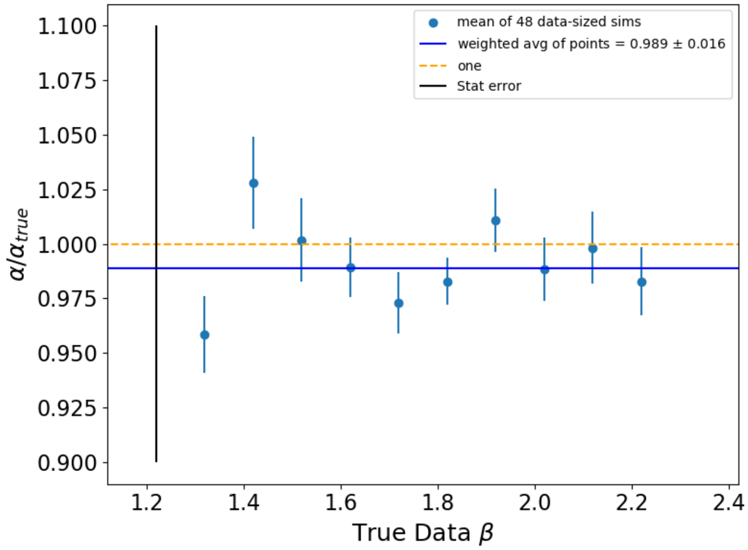

Figure 4.7: The x-axis shows the “true” β for the simulated data-sized samples on which the rate method is validated. The position on the y axis for each dot shows how different the mean of the fit k over the 48 data-sized simulated samples at each “true” β were from the true k in the simulation. All of these used a MC comparison sim with $\beta = 1.82$ as found in this work

CHAPTER 5

RESULTS

In this chapter I present my results. I begin by showing the redshift distribution of the data sample and other quantities relevant to the rate analysis in §5.1. Then I describe the systematic tests of the analysis in §5.2. This includes the test of different Core Collapse spectral models in §5.2.1, the test of variation in redshift range of the analysis in §5.2.2, and the test of light curve quality cut variation in §5.2.3. Then in §5.3, I present my results. First I describe the analysis that I performed while blinded along with the state of the nominal analysis before unblinding, and major changes post-unblinding in §5.3.1. Then I describe the results obtained using a low redshift prior from the SDSS Dilday et al. 2010 analysis in §5.3.2. Finally, I provide my final results in §5.3.3 including a comparison with prior sky survey rate analyses.

5.1 Data Sample Level Results

In figure 5.1 I show the distribution of photometric redshift for the data sample (black dots) and simulation (orange for all SNe and blue for SN-CC only) with the same cuts used in the nominal analysis and the best fit rate parameters for the simulation.

In figure 5.2 I show the ratio of the photometric redshift distribution between data and simulation (blue dots) and the best fit (blue) line to those points along with a comparison (red) line at the ideal ratio of 1:1.

These two figures show that the rate parameters of the simulation plotted here (same as the best-fit rate parameters) describe the data sample well. The slope of the line in figure 5.2 does not need to be equal to 1.0 to be the best fit for the data since the linear fit is only an approximation, both to the power law form of the rate law and the model described in §3.

Figure 5.3 shows the fraction of events which are true simulated core collapse or peculiar

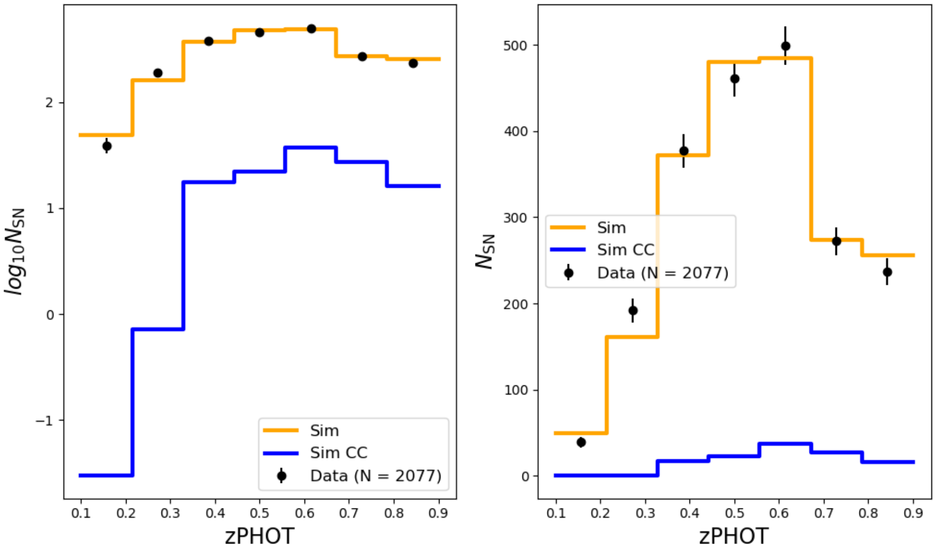

Figure 5.1: Photometric redshift distribution for the data sample (dots), entire simulated sample (orange lines), and simulated core collapse supernovae only (blue lines). Left panel is a logarithmic scale and the right panel is a linear scale.

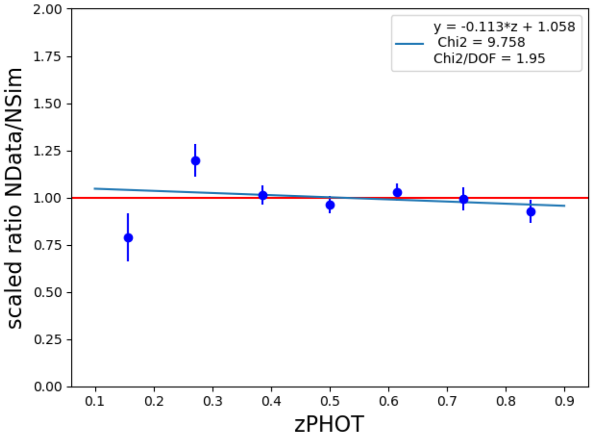

Figure 5.2: Ratio between data photometric redshift distribution and simulation photometric redshift distribution (blue dots). The best fit trend line to that ratio vs redshift is also in blue. The ideal ratio of 1:1 is shown as a red line for comparison.

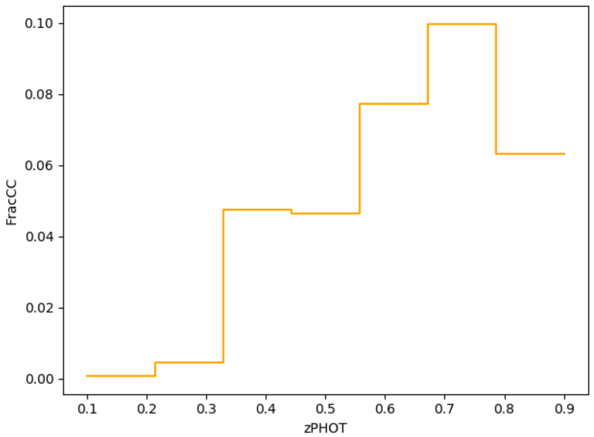

Figure 5.3: Fraction of events which are core collapse vs. photometric redshift predicted by simulations after the scaling described in §3.1.1.

SNe Ia vs photometric redshift. This sharp increase in CC Fraction with redshift is not due to real CC supernovae that we observe at those redshifts, but rather a set of low redshift core collapse SNe that are so faint that they are well-fit by a high photometric redshift SN Ia.

5.2 Systematic Tests

In this section I describe the systematic tests I conduct on the analysis. They include tests of the core collapse contamination model used in the simulations in §5.2.1, tests of the redshift range of the analysis in §5.2.2, and tests of the light curve quality cut selection in §5.2.3. At the end of this section in §5.2.4, I show a table summarizing all the systematic tests and their effects on the rate fit parameters.

5.2.1 Core Collapse Models

While the model outlined in Jones et al. 2017 (104) that we use in the nominal analysis (J17a) is a good representation of the core collapse observed in the PS1 survey, it is not necessarily the true model. However, there are several other models available that have been demonstrated to match observed data samples well. These include the model from Kessler et al. 2010 (105) (K10), the model from Jones et al. 2017 before the magnitudes were adjusted to match the Li et al. 2011 (46) Luminosity function (J17b), and a recently published set of templates from Vincenzi et al. 2019 (106) (V19).

In order to test the effects of the core collapse model on the rate fit, we simulate a MC comparison sample using each of these models and fit the data using those MC samples. To compare the size of this effect to any statistical effects introduced by using a different MC sample, we also fit the set of 48 data-sized sims using the nominal (J17a) core collapse model and compare the RMS of the change in power law fit parameters between the nominal and systematic CC models. The results of this systematic are shown in Tables 5.3 and 5.4 and graphically in Figures 5.4 and 5.5.

5.2.2 Redshift Range of Analysis

Most prior rate analyses (1; 2; 3) use a powerlaw in (1+z) for the lower redshift range. However, analyses including Perrett et al. 2012 (3) find that their data is better fit by a power law which levels off after z = 1.0. Other non-parametric rate analyses (70; 71) find that their measured rate stops increasing around z = 1.0.

In addition to the potential for varying true supernova rate models at high redshifts, we also suffer from lower statistics in both the lowest (z = 0.1-0.2) and highest (z = 0.9-1.0, 1.0-1.1, and 1.1-1.2) redshift bins that could result in poor fits when including those bins. Therefore, we test the effect of changing the redshift fit range on the fit rate parameters. We examine the effect of removing the lowest z bin as well as sequentially adding on the redshift bins beyond z = 0.9. As with the earlier systematics, the results are shown in Tables 5.4 and 5.3 and graphically in Figures 5.5 and 5.4.

5.2.3 Light Curve Quality Cuts

The nominal analysis used similar light curve quality cuts as the DES3YR analysis, a cosmology analysis performed on the set of spectroscopically confirmed type Ia supernovae. Since this analysis deals with an impure sample of SNe Ia, we consider the use of stricter cuts that

Cuts	FITPROB	SNRMAX cut	NEPOCH cut
Nominal	0.1	5	5
Systematic	0.01	8	10

Table 5.1: Table showing values of different LC parameter cuts for the nominal analysis and the systematic tests.

can reduce the core collapse contamination fraction as systematics and weaker cuts that can increase the sample size. Table 5.1 shows the nominal and systematic cuts. Each systematic cut is applied separately so that its individual effect on the fit can be analyzed.

5.2.4 Summary of Systematic Uncertainties

Table 5.2 shows the summary statistics for each of the systematic tests and the nominal. These statistics include $R_{\text{data/sim}}$, the ratio of data/sim events in the systematic relative to the nominal, data/sim χ^2/DOF, the χ^2 of the best fit power law rate model to the data/sim respectively and the number of degrees of freedom (Number of bins - 2 rate fit parameters), and Frac CC Unscaled/Scaled, the percentage of simulated events passing all cuts that are Core Collapse before/after applying the scaling described in §3.1.1.

Table 5.3 shows the shift in β for each systematic test and Table 5.4 shows the shift in k for each systematic test. For those tables, $\Delta\beta$ is the shift in beta value between nominal and systematic ($\Delta\beta = \beta_{\text{nom}} - \beta\text{sys}$) and R_{k} is the ratio between nominal and systematic k ($R_{\text{k}} = \frac{k_{\text{nom}}}{k_{\text{sys}}}$). The σ_{stat} column in each table shows the statistical error on each parameter for the data for each systematic or the mean statistical error over 48 sims for each systematic. The μ column shows the mean difference in parameters between 48 sims each fit once with the nominal and once with the systematic. Similarly, the σ columns are the standard error in the mean of that difference over the 48 sims.

The systematic shifts are summarized graphically below in Figure 5.4 for β and Figure 5.5 for k. The large and increasing CC fraction at high redshift as shown in Figure 5.3 can contribute to variance at high redshift and could be a reason why the redshift range systematics are the most significant.

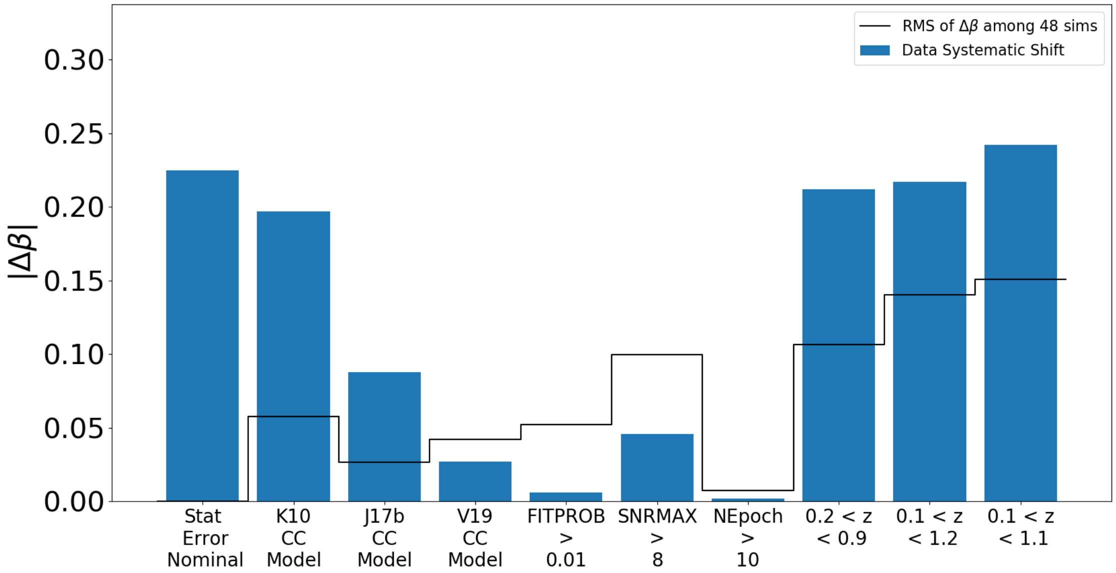

Figure 5.4: Absolute value of shift in β for each systematic test (blue bars). Compared to RMS shift of β over 48 simulated DES-sized simulations(black line)

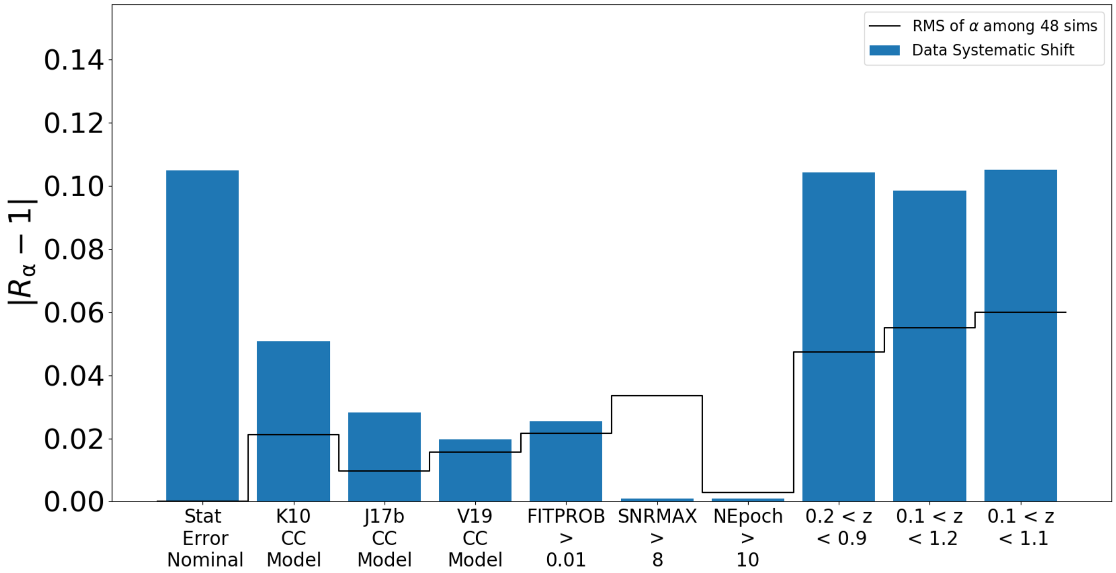

Figure 5.5: Absolute value of fractional shift in k for each systematic test (blue bars). Compared to RMS fractional shift of k over 48 simulated DES-sized simulations (black line)

Systematic	$R_{\rm data}$	Data χ^2/DOF	$R_{\rm sim}$	Mean Sim χ^2/DOF	Frac CC Unscaled	Frac CC Scaled
Nominal	1.00	13.951/ 6	1.00	7.216 / 6	0.067	0.078
K10 CC Model	1.000	16.724 / 6	1.00	8.643 / 6	0.018	0.029
J17b CC Model	1.000	15.478 / 6	1.00	7.343 / 6	0.024	0.057
V19 CC Model	1.000	16.262 / 6	1.00	7.589 / 6	0.022	0.040
FITPROB > 0.01	1.075	17.401 / 6	1.05	7.041 / 6	0.083	0.094
SNRMAX > 8	0.807	16.162 / 6	0.83	7.565 / 6	0.045	0.058
NEpoch > 10	1.000	13.963 / 6	1.00	7.238 / 6	0.067	0.078
0.2 < z < 0.9	0.987	11.948 / 5	0.98	6.517 / 5	0.068	0.077
0.1 < z < 1.2	1.087	20.383 / 9	1.09	9.888 / 9	0.073	0.080
0.1 < z < 1.1	1.066	21.253 / 8	1.08	9.370 / 8	0.072	0.081

Table 5.2: Summary statistics for the systematic tests described in §5.2.4

Systematic	$\Delta\beta_{\rm data}$	$\sigma_{\rm stat}\Delta\beta_{\rm data}$	$\mu\Delta\beta_{\rm sims}$	$\sigma\Delta\beta_{\rm sims}$	$\sigma_{\rm stat}\Delta\beta_{\rm sims}$
Nominal	0.0	0.225	0.0	—	0.264
K10 CC Model	-0.197	0.194	-0.294	0.008	0.208
J17b CC Model	-0.088	0.217	-0.147	0.004	0.244
V19 CC Model	-0.027	0.212	-0.129	0.006	0.232
FITPROB > 0.01	-0.006	0.212	-0.018	0.008	0.270
SNRMAX > 8	0.046	0.237	-0.013	0.015	0.289
NEpoch > 10	0.002	0.225	-0.000	0.001	0.265
0.2 < z < 0.9	0.212	0.261	0.003	0.016	0.272
0.1 < z < 1.2	0.217	0.208	-0.025	0.020	0.209
0.1 < z < 1.1	0.242	0.213	-0.020	0.022	0.206

Table 5.3: Effect of systematic tests described above on the power law index β.

Systematic	$R_{\rm K,data}$	$\sigma_{stat}R_{\rm K,data}$	$\mu R_{\rm K,sim}$	$\sigma R_{\rm K,sim}$	$\sigma_{stat}R_{\rm K,sim}$
Nominal	1.0	0.105	1.0	—	0.133
K10 CC Model	0.949	0.090	1.093	0.003	0.103
J17b CC Model	0.972	0.100	1.054	0.001	0.120
V19 CC Model	1.020	0.104	1.027	0.002	0.118
FITPROB > 0.01	1.025	0.102	1.009	0.003	0.133
SNRMAX > 8	1.001	0.109	1.005	0.005	0.145
NEpoch > 10	1.001	0.105	1.000	0.000	0.133
0.2 < z < 0.9	1.104	0.134	0.998	0.007	0.137
0.1 < z < 1.2	1.099	0.108	1.011	0.008	0.101
0.1 < z < 1.1	1.105	0.110	1.009	0.009	0.099

Table 5.4: Effect of systematic tests described above on the power law normalization k.

In each of the above plots, the first blue bar represents the size of the statistical error on the parameter in the nominal analysis. The remaining blue bars represent the systematic shift in each parameter for the systematic test listed below. The black line shows the RMS variation in each parameter due to the systematic test among the 48 datasized simulations.

We only consider the systematic shifts as part of the systematic error if the shift is larger than the RMS variation (i.e. if the blue bar exceeds the black line).

The systematic tests are grouped into sets of similar tests. First are the changes in core collapse model in the comparison simulation, second are the variation in LC quality cuts, and last is the variation in redshift range of the analysis. While we count data systematics that surpass the simulation RMS as part of the systematic error, we do not double count systematics in the same group since they are testing the same part of the analysis and are therefore not orthogonal errors.

5.3 Rate Results

5.3.1 Blinded Analysis

Before April 30, 2020, the rate fit parameter outputs were blinded. This means that before the results were output to human-readable files, an unknown number equal to the cosine of a very large number was added to them to make it impossible to consciously or subconsciously modify the output to make it in better agreement with prior analyses. Since this number was always the same, it was possible to check systematic tests for consistency while blinded as well as check unblinded parameters such as the statistical errors and core collapse scale factors (see §3.1.1).

On that date, the blinding was removed and the results were recorded here including the best-fit rate model and all of the systematic test results. Those systematic tests are shown below in Tables 5.5, 5.6, and 5.7.

Table 5.5 shows several summary statistics for the nominal analysis and a set of systematics. These systematics include different CC supernova templates (K10, J17b), variations on light curve fit parameter cuts (FITPROB > 0.01, SNRMAX > 8, and NEpoch> 10), and different redshift ranges to fit ($0.2 < z < 0.9$, etc).

The summary statistics in that first table are, in order, are average number of simulated

SNe in the data sized simulations used in the rate fit, Number of data SNe used in the rate fit, what fraction of the simulated supernovae that passed all cuts were core collapse, and the best fit χ^2 for both the Data and Sim rate fit.

Tables 5.6 and 5.7 show systematic variation in the normalization parameter K and the power law index β respectively. Those columns are, in order, mean change of the parameter between Nominal and the given systematic over 48 data-sized sims, standard deviation of the change in the parameter between Nominal and the given systematic over the same 48 data sized sims, Average statistical error on the parameter over the 48 data-sized sims, shift in the best fit parameter for the data between the nominal and the systematic, and the statistical error on the parameter from the data.

The Nominal analysis at that time used:

- LC Quality Cuts
  - Mostly consistent with the cuts used in the DES-3YR analysis (Brout et al. 2020a)
  - Major difference is that we cut events with FITPROB > 0.1 rather than 0.01
  - To test the effects of this change, we include the original FITPROB > 0.01 cut as a systematic
- Classification
  - We use the three parameter (z, c, x1) SNANA Radius Nearest Neighbor classifier described in §2.4 trained with $\Delta_{\mathrm{z}} = 0.0500$, $\Delta_{\mathrm{c}} = 0.0600$, and $\Delta_{\mathrm{x1}} = 0.5000$
- Rate Fit parameters
  - Redshift range is $0.1 < \mathrm{z} < 0.9$
  - All fits, both nominal and systematic redshift ranges, use redshift bin sizes of 0.1. This is comparable to the uncertainty in photometric redshifts.

  - Definition of “Hubble Residual Tail” used in the Core Collapse Contamination scale determination (§3.1.1) is $|MURES| > 1$. That scale determination is performed in 3 redshift bins
  - 5 iterations of fit for rate followed by fit CC scale are performed. This is to ensure convergence since the CC scale depends on power law index of the rate.

- Core Collapse Supernova Models
  - CC Supernova rate in simulations is taken from Strolger et al. 2015
  - CC spectral templates are taken from Jones et al. 2017 after a 1.1 magnitude brightening of the Type II templates and a 1.2 magnitude brightening of the Type Ibc templates in order to match the Li et al. 2011 Luminosity function
  - The Jones et al. 2017 model without the adjustment (J17b) and the Kessler et al. 2010 models (K10) are included as systematic tests.

For a rate model where SN Rate $= k \times (1+z)^{\beta}$, we find immediately post unblinding that

k = 1.88x 10^{-5} $\pm 0.23(stat) \pm 0.32(sys)$ SNe yr^{-1} Mpc^{-3} h_{70}^{-3}

$\beta = 1.61 \pm 0.22(stat) \pm 0.26(sys)$

Below is a list of the changes made to the analysis post-unblinding:

- The MC Comparison simulations were rerun with a different solid angle to correct for the losses in area discussed in section 3.2.
- SNANA light curve fitting code was updated to correct a bug with the photo-z fitting which had previously caused an erroneous spike in photo-z errors at 0.05
- Input x1 distribution was shifted by -0.18 from the Scolnic and Kessler 2016 distribution to match the data.

Systematic	$N_{sim}/N_{sim,Nom}$	$N_{data}/N_{data,Nom}$	Frac CC	Data χ^2/DOF	Mean Sim χ^2/DOF
Nominal	1.00	1.00	0.079	1.535	0.926
K10 CC Model	1.000	1.000	0.021	1.647	1.077
J17b CC Model	1.000	1.000	0.030	1.577	0.961
FITPROB > 0.01	0.931	1.092	0.064	1.846	0.953
SNRMAX > 8	0.814	0.794	0.060	1.664	0.945
NEpoch > 10	1.000	1.000	0.079	1.534	0.925
0.2 < z < 0.9	0.984	0.980	0.081	1.431	0.893
0.1 < z < 1.2	1.096	1.089	0.085	1.628	0.938
0.1 < z < 1.1	1.082	1.069	0.083	1.730	0.952

Table 5.5: Summary of data and sim content for systematics immediately post unblinding

Systematic	$\mu K_{sims}/K_{Nom}$	$\sigma K_{sims}/K_{Nom}$	$\sigma_{stat} K_{sims}/K_{ref}$	K_{data}/K_{Nom}	$\sigma_{stat} K_{data}/K_{ref}$
Nominal	1.0	—	0.113	1.0	0.115
K10 CC Model	1.069	0.004	0.086	1.034	0.102
J17b CC Model	1.024	0.001	0.102	1.017	0.110
FITPROB > 0.01	1.001	0.004	0.112	0.976	0.112
SNRMAX > 8	1.010	0.005	0.110	1.005	0.118
NEpoch > 10	1.000	0.000	0.114	0.998	0.115
0.2 < z < 0.9	0.997	0.007	0.119	0.885	0.155
0.1 < z < 1.2	0.991	0.007	0.096	0.945	0.111
0.1 < z < 1.1	0.993	0.007	0.097	0.940	0.114

Table 5.6: Summary of Systematic tests on K immediately post unblinding

Systematic	$\mu\Delta\beta_{sims}$	$\sigma\Delta\beta_{sims}$	$\sigma_{stat}\Delta\beta_{sims}$	$\Delta\beta_{data}$	$\sigma_{stat}\Delta\beta_{data}$
Nominal	0.0	—	0.246	0.0	0.230
K10 CC Model	-0.264	0.010	0.187	-0.175	0.198
J17b CC Model	-0.095	0.004	0.223	-0.073	0.219
FITPROB > 0.01	-0.004	0.009	0.244	-0.002	0.218
SNRMAX > 8	-0.028	0.014	0.244	0.049	0.241
NEpoch > 10	-0.000	0.001	0.247	0.003	0.230
0.2 < z < 0.9	0.009	0.014	0.263	0.263	0.277
0.1 < z < 1.2	0.023	0.017	0.202	0.103	0.203
0.1 < z < 1.1	0.017	0.018	0.204	0.132	0.209

Table 5.7: Summary of Systematic tests on β immediately post unblinding

5.3.2 SDSS Priors

In addition to using the DES-SN sample, we performed a parallel analysis where we added a prior to the χ^2 based on the 2010 SDSS low-z rate analysis. This additional low-z constraint was expected to improve our measurement due to our relatively small low-z sample.

Below are the same tables showing results of the systematic tests for the analysis with

SDSS Priors as shown above in §5.2 for the nominal results.

Systematic	R_{data}	Data χ^2/DOF	R_{sim}	Mean Sim χ^2/DOF	Frac CC Unscaled	Frac CC Scaled
Nominal	1.00	14.089/ 7	1.00	7.484 / 7	0.067	0.078
K10 CC Model	1.000	17.055 / 7	1.000	9.086 / 7	0.018	0.029
J17b CC Model	1.000	15.735 / 7	1.000	7.715 / 7	0.024	0.057
FITPROB > 0.01	1.075	17.441 / 7	1.049	7.323 / 7	0.083	0.094
SNRMAX > 8	0.807	16.303 / 7	0.825	7.849 / 7	0.045	0.058
NEpoch > 10	1.000	14.096 / 7	1.000	7.506 / 7	0.067	0.078
0.2 < z < 0.9	0.987	11.957 / 6	0.982	6.888 / 6	0.068	0.077
0.1 < z < 1.2	1.087	20.409 / 10	1.091	10.095 / 10	0.073	0.079
0.1 < z < 1.1	1.066	21.327 / 9	1.078	9.370 / 9	0.072	0.081

Table 5.8: Summary statistics for the systematic tests described in in §5.2.4 when including the SDSS low-z prior.

Systematic	$\Delta\beta_{\text{data}}$	$\sigma_{\text{stat}}\Delta\beta_{\text{data}}$	$\mu\Delta\beta_{\text{sims}}$	$\sigma\Delta\beta_{\text{sims}}$	$\sigma_{\text{stat}}\Delta\beta_{\text{sims}}$
Nominal	0.0	0.195	0.0	—	0.231
K10 CC Model	-0.181	0.171	-0.260	0.007	0.183
J17b CC Model	-0.074	0.189	-0.122	0.003	0.212
FITPROB > 0.01	-0.027	0.187	-0.013	0.006	0.236
SNRMAX > 8	0.053	0.205	-0.010	0.012	0.251
NEpoch > 10	0.001	0.195	-0.000	0.001	0.231
0.2 < z < 0.9	0.158	0.225	0.001	0.011	0.231
0.1 < z < 1.2	0.172	0.187	-0.023	0.016	0.183
0.1 < z < 1.1	0.196	0.192	-0.029	0.019	0.206

Table 5.9: Effect of systematic tests described above on the power law index β when including the SDSS Prior.

Systematic	$R_{\text{K,data}}$	$\sigma_{stat}R_{\text{K,data}}$	$\mu R_{\text{K,sim}}$	$\sigma R_{\text{K,sim}}$	$\sigma_{stat}R_{\text{K,sim}}$
Nominal	1.0	0.091	1.0	—	0.113
K10 CC Model	0.957	0.080	1.075	0.002	0.090
J17b CC Model	0.979	0.087	1.041	0.001	0.103
FITPROB > 0.01	1.015	0.089	1.007	0.002	0.113
SNRMAX > 8	1.004	0.093	1.003	0.004	0.122
NEpoch > 10	1.001	0.091	1.000	0.000	0.114
0.2 < z < 0.9	1.076	0.112	0.998	0.005	0.114
0.1 < z < 1.2	1.074	0.095	1.009	0.006	0.088
0.1 < z < 1.1	1.079	0.097	1.013	0.007	0.099

Table 5.10: Effect of systematic tests described above on the power law normalization k when including the SDSS prior.

The systematic shifts are summarized graphically below in Figure 5.6 for β and Figure 5.7 for k. The figure descriptions are identical to those for Figures 5.4 and 5.5

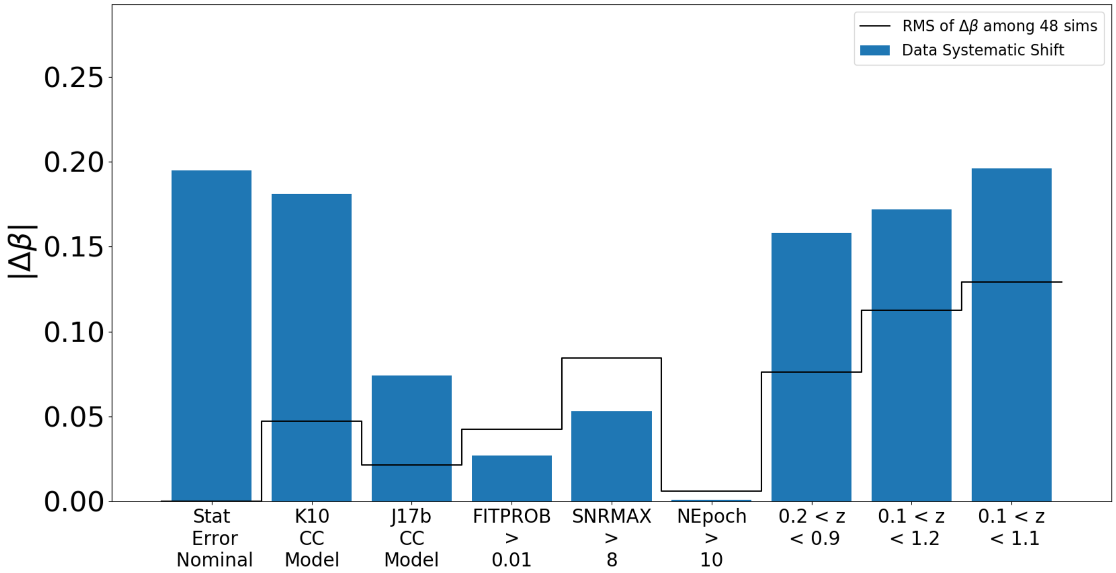

Figure 5.6: Absolute value of shift in β for each systematic test when including the SDSS prior (blue bars). Compared to RMS shift of β over 48 simulated DES-sized simulations(black line)

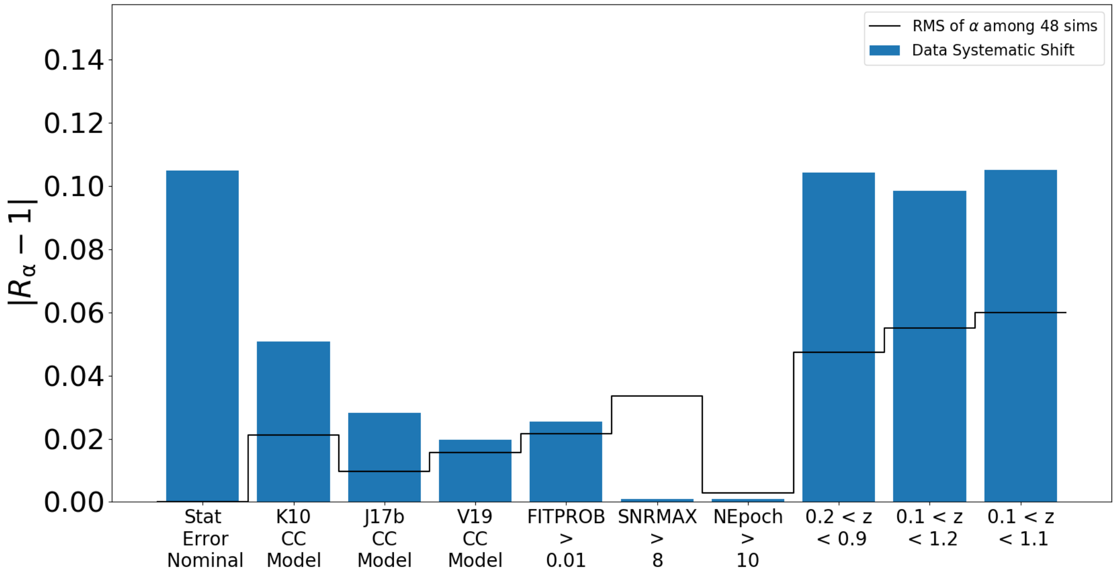

Figure 5.7: Absolute value of fractional shift in k for each systematic test when including the SDSS prior (blue bars). Compared to RMS fractional shift of k over 48 simulated DES-sized simulations (black line)

5.3.3 Final Results

Fitting the data to a power law in the form $\alpha(1+z)^{\beta}$, we obtain $\alpha =$ 2.00± 0.21(stat) ± 0.24(sys) and β = 1.82± 0.23(stat) ± 0.31(sys).

Due to our small sample size in the lowest redshift bin, we also explore the effect of adding a prior from the Dilday et al. 2010 (2) rate analysis at z = 0.12. In that case, we obtain α = 2.03± 0.19(stat) ± 0.18(sys) and β = 1.79± 0.20(stat) ± 0.27(sys).

Those results, along with the results from Dilday et al. 2008, Dilday et al. 2010, Perrett et al. 2012, Frohmaier et al. 2019, and our result with and without SDSS priors are detailed in the table below (1; 2; 3).

Survey	α (10^{-5} SN/yr/Mpc^{-3})	Stat. Err	Sys. Err	β	Stat. Err	Sys. Err	$\rho_{\alpha\beta}$
SDSS + SNLS (spec) + SCP + GOODS + Cappellaro 99 (D08)	2.6	0.55	—	1.5	0.6	—	-0.8
SDSS (D10)	2.32	0.15	—	2.04	0.9	—	-0.02
SNLS (P12)	1.7	0.3	—	2.11	0.28	—	—
SNLS + LOSS + SDSS + SDF (P12)	2.1	0.1	—	1.70	0.12	—	—
PTF + SDSS + SNLS + Subaru + CANDELS (F19)	2.27	0.19	—	1.70	0.21	—	—
DES (this work)	2.00	0.21	0.24	1.82	0.23	0.31	-0.97
DES + SDSS Priors (this work)	2.03	0.19	0.18	1.79	0.20	0.27	-0.96

Table 5.11: Comparison of results with prior rate analysis results

In addition to the previously defined rate fit parameters, $\rho_{\alpha,\beta}$ is the correlation coefficient between the two power law rate parameters α and β. This indicates that for our analysis, α and β are nearly perfectly anti-correlated.

As in all prior rate analyses we find that the SN Ia rate is increasing with redshift at a $> 6\sigma$ significance with statistical errors only and a 4.7σ significance overall. We find that both of our parameters α and β are consistent with all prior analyses within 1σ.

Our χ^2 of 13.95 with 6 degrees of freedom provides a probability to exceed of 3%. In combination with Figure 5.8 showing that one data-sized simulation out of a set of 100

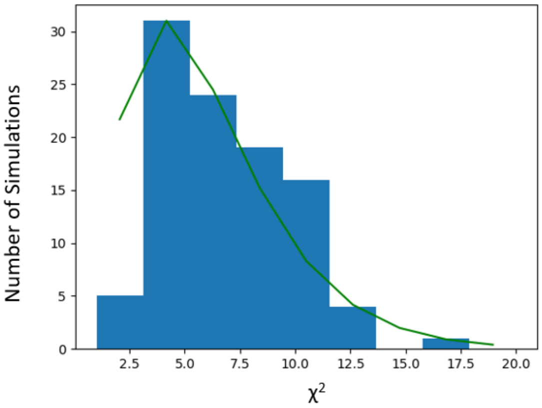

Figure 5.8: Distribution of best fit χ^2 values for a set of 100 data-sized simulations (blue). The χ^2 distribution for 100 samples and six degrees of freedom is overplotted in green.

simulations are fit with at least that high of a χ^2, we can say that this data is reasonably well-fit by a power law rate model.

CHAPTER 6

CONCLUSION

We presented the first major science analysis using the full 5 year DES-SN data sample. We have tuned simulation parameters to match the sample in color, stretch, and ultimately redshift distribution. We analyzed the the quality of the photometric redshift fit in the data using a subsample of events with host galaxy spectra and we also validated the photometric redshift fit on simulations with that subsample. We have shown results that are consistent with all prior rate analyses and which have a lower statistical error while being the first analysis to perform a systematic test specifically on the power law rate analysis. Our statistical errors are nearly as much lower than the SNLS-only analysis as would be expected with our 3-fold increase in sample size despite using no spectroscopic information in our analysis.

This analysis, while complete in its own scope, can still be expanded in several ways. We plan on conducting an analysis which will constrain the delay time distribution using these rate measurements and which will be able to shed more light on the SN progenitor dilemma. Additionally, our large sample of 2077 Supernovae will enable us to perform fits using subsamples of data such as the high-low stretch split performed by Perrett et al. 2012 and potentially other splits involving host galaxy properties.

REFERENCES

[1] B. Dilday, R. Kessler, J. A. Frieman, *et al.*, "A Measurement of the Rate of Type Ia Supernovae at Redshift z $\approx$ 0.1 from the First Season of the SDSS-II Supernova Survey," *Astrophysical Journal*, vol. 682, pp. 262–282, Jul 2008.

[2] B. Dilday, M. Smith, B. Bassett, *et al.*, "Measurements of the Rate of Type Ia Supernovae at Redshift $\approx$ 0.3 from the Sloan Digital Sky Survey II Supernova Survey," *ApJ*, vol. 713, pp. 1026–1036, Apr 2010.

[3] K. Perrett, M. Sullivan, A. Conley, *et al.*, "Evolution in the Volumetric Type Ia Supernova Rate from the Supernova Legacy Survey," *AJ*, vol. 144, p. 59, Aug 2012.

[4] W. Baade, "The Absolute Photographic Magnitude of Supernovae.," *Astrophysical Journal*, vol. 88, p. 285, Oct. 1938.

[5] R. Minkowski, "Supernovae and Supernova Remnants," *Annual Review of Astronomy and Astrophysics*, vol. 2, p. 247, Jan. 1964.

[6] C. T. Kowal, "Absolute magnitudes of supernovae.," *Astronomical Journal*, vol. 73, pp. 1021–1024, Dec. 1968.

[7] D. Branch and C. Bettis, "The Hubble diagram for supernovae.," *Astronomical Journal*, vol. 83, pp. 224–227, Mar. 1978.

[8] A. Sandage and G. A. Tammann, "Steps toward the Hubble constant. VIII - The global value," *Astrophysical Journal*, vol. 256, pp. 339–345, May 1982.

[9] M. Capaccioli, E. Cappellaro, *et al.*, "Distances of the Virgo and Coma Clusters of Galaxies through Novae and Supernovae," *Astrophysical Journal*, vol. 350, p. 110, Feb. 1990.

[10] G. A. Tammann and B. Leibundgut, “Supernova studies. IV. The global value of HO from supernovae IA and the peculiar motion of field galaxies.,” *Astronomy and Astrophysics*, vol. 236, p. 9, Sept. 1990.

[11] A. Sandage and G. A. Tammann, “The Hubble Diagram in V for Supernovae of Type IA and the Value of H 0 Therefrom,” *Astrophysical Journal*, vol. 415, p. 1, Sept. 1993.

[12] M. M. Phillips, “The Absolute Magnitudes of Type IA Supernovae,” *Astrophysical Journal Letters*, vol. 413, p. L105, Aug. 1993.

[13] Y. P. Pskovskii, “The Photometric Properties of Supernovae.,” *Soviet Astronomy*, vol. 11, p. 63, Aug. 1967.

[14] I. P. Pskovskii, “Light curves, color curves, and expansion velocity of type I supernovae as functions of the rate of brightness decline,” *Soviet Astronomy*, vol. 21, p. 675, Dec. 1977.

[15] Y. P. Pskovskii, “Photometric classification and basic parameters of type I supernovae,” *Soviet Astronomy*, vol. 28, pp. 658–664, Dec. 1984.

[16] R. Tripp, “A two-parameter luminosity correction for Type IA supernovae,” *Astronomy and Astrophysics*, vol. 331, pp. 815–820, Mar. 1998.

[17] A. G. Riess, A. V. Filippenko, P. Challis, *et al.*, “Observational Evidence from Supernovae for an Accelerating Universe and a Cosmological Constant,” *AJ*, vol. 116, pp. 1009–1038, Sep 1998.

[18] B. P. Schmidt, N. B. Suntzeff, M. M. Phillips, *et al.*, “The High-Z Supernova Search: Measuring Cosmic Deceleration and Global Curvature of the Universe Using Type IA Supernovae,” *Astrophysical Journal*, vol. 507, pp. 46–63, Nov. 1998.

[19] S. Perlmutter, G. Aldering, G. Goldhaber, *et al.*, “Measurements of Ω and Λ from 42 High-Redshift Supernovae,” *ApJ*, vol. 517, pp. 565–586, Jun 1999.

[20] J. A. Frieman, B. Bassett, A. Becker, *et al.*, "The Sloan Digital Sky Survey-II Supernova Survey: Technical Summary," *AJ*, vol. 135, pp. 338–347, Jan 2008.

[21] M. Sako, B. Bassett, A. Becker, *et al.*, "The Sloan Digital Sky Survey-II Supernova Survey: Search Algorithm and Follow-up Observations," *AJ*, vol. 135, pp. 348–373, Jan 2008.

[22] M. Sullivan and Supernova Legacy Survey Collaboration, *The Supernova Legacy Survey*, vol. 342 of *Astronomical Society of the Pacific Conference Series*, p. 466. 2005.

[23] B. Granett, K. Chambers, and E. Magnier, "The Pan-STARRS Imaging Sky Probe," in *The Advanced Maui Optical and Space Surveillance Technologies Conference*, p. E45, Jan 2006.

[24] J. Frieman and Dark Energy Survey Collaboration, "The Science of the Dark Energy Survey," in *American Astronomical Society Meeting Abstracts*, vol. 205 of *American Astronomical Society Meeting Abstracts*, p. 69.15, Dec 2004.

[25] A. G. Riess, L. M. Macri, S. L. Hoffmann, *et al.*, "A 2.4% Determination of the Local Value of the Hubble Constant," *Astrophysical Journal*, vol. 826, p. 56, July 2016.

[26] W. L. Freedman, B. F. Madore, D. Hatt, *et al.*, "The Carnegie-Chicago Hubble Program. VIII. An Independent Determination of the Hubble Constant Based on the Tip of the Red Giant Branch," *Astrophysical Journal*, vol. 882, p. 34, Sept. 2019.

[27] R. J. Foley, R. Hounsell, D. Scolnic, and WFIRST Supernova Science Investigation Team, "The WFIRST Supernova Survey," in *American Astronomical Society Meeting Abstracts #229*, vol. 229 of *American Astronomical Society Meeting Abstracts*, p. 406.07, Jan 2017.

[28] Ž. Ivezić, S. M. Kahn, J. A. Tyson, *et al.*, "LSST: From Science Drivers to Reference

Design and Anticipated Data Products," *Astrophysical Journal*, vol. 873, p. 111, Mar. 2019.

[29] W. M. Wood-Vasey, P. Pinto, L. Wang, H. Zhan, Y. Wang, and LSST Supernova Science Collaboration, "Supernova Science and Cosmology with the LSST," in *American Astronomical Society Meeting Abstracts*, vol. 209 of *American Astronomical Society Meeting Abstracts*, p. 86.11, Dec 2006.

[30] J. Whelan and J. Iben, Icko, "Binaries and Supernovae of Type I," *ApJ*, vol. 186, pp. 1007–1014, Dec 1973.

[31] M. Livio and A. G. Riess, "Have the Elusive Progenitors of Type Ia Supernovae Been Discovered?," *ApJ*, vol. 594, pp. L93–L94, Sep 2003.

[32] A. V. Tutukov, A. V. Fedorova, and L. R. Yungelson, "The evolution of dwarf binaries," *Soviet Astronomy Letters*, vol. 8, pp. 198–201, Jun 1982.

[33] R. F. Webbink, "Double white dwarfs as progenitors of R Coronae Borealis stars and type I supernovae.," *ApJ*, vol. 277, pp. 355–360, Feb 1984.

[34] J. Iben, I. and A. V. Tutukov, "On the evolution of close binaries with components of initial mass between 3 M and 12 M.," *ApJs*, vol. 58, pp. 661–710, Aug 1985.

[35] T. A. Thompson, "Accelerating Compact Object Mergers in Triple Systems with the Kozai Resonance: A Mechanism for "Prompt" Type Ia Supernovae, Gamma-Ray Bursts, and Other Exotica," *ApJ*, vol. 741, p. 82, Nov 2011.

[36] M. M. Phillips, P. Lira, N. B. Suntzeff, *et al.*, "The Reddening-Free Decline Rate Versus Luminosity Relationship for Type IA Supernovae," *Astronomical Journal*, vol. 118, pp. 1766–1776, Oct. 1999.

[37] DES Collaboration, "First Cosmology Results using Type Ia Supernovae from the

Dark Energy Survey: Constraints on Cosmological Parameters," *Astrophysical Journal Letters*, vol. 872, p. L30, Feb. 2019.

[38] S. Dhawan, B. Leibundgut, J. Spyromilio, and S. Blondin, "A reddening-free method to estimate the ^{56}Ni mass of Type Ia supernovae," *Astronomy and Astrophysics*, vol. 588, p. A84, Apr. 2016.

[39] M. Livio and P. Mazzali, "On the progenitors of Type Ia supernovae," *Physics Reports*, vol. 736, pp. 1–23, Mar 2018.

[40] G. H. Marion, P. J. Brown, J. Vinkó, *et al.*, "SN 2012cg: Evidence for Interaction Between a Normal Type Ia Supernova and a Non-degenerate Binary Companion," *Astrophysical Journal*, vol. 820, p. 92, Apr. 2016.

[41] O. Graur, D. Zurek, M. M. Shara, *et al.*, "Late-time Photometry of Type Ia Supernova SN 2012cg Reveals the Radioactive Decay of 57 Co," *Astrophysical Journal*, vol. 819, p. 31, Mar. 2016.

[42] W. Li, X. Wang, M. Hu, *et al.*, "Observations of Type Ia Supernova 2014J for Nearly 900 Days and Constraints on Its Progenitor System," *Astrophysical Journal*, vol. 882, p. 30, Sept. 2019.

[43] K. Maguire, M. Sullivan, F. Patat, *et al.*, "A statistical analysis of circumstellar material in Type Ia supernovae," *Monthly Notices of the Royal Astronomical Society*, vol. 436, pp. 222–240, Nov. 2013.

[44] A. Sternberg, A. Gal-Yam, J. D. Simon, *et al.*, "Circumstellar Material in Type Ia Supernovae via Sodium Absorption Features," *Science*, vol. 333, p. 856, Aug. 2011.

[45] K. Nomoto and S.-C. Leung, "Single Degenerate Models for Type Ia Supernovae: Progenitor's Evolution and Nucleosynthesis Yields," *Space Science Reviews*, vol. 214, p. 67, June 2018.

[46] W. Li, J. S. Bloom, P. Podsiadlowski, *et al.*, “Exclusion of a luminous red giant as a companion star to the progenitor of supernova SN 2011fe,” *Nature*, vol. 480, pp. 348–350, Dec 2011.

[47] P. L. Kelly, O. D. Fox, A. V. Filippenko, *et al.*, “Constraints on the Progenitor System of the Type Ia Supernova 2014J from Pre-explosion Hubble Space Telescope Imaging,” *ApJ*, vol. 790, p. 3, Jul 2014.

[48] J. I. González Hernández, P. Ruiz-Lapuente, *et al.*, “No surviving evolved companions of the progenitor of SN 1006,” *Nature*, vol. 489, pp. 533–536, Sept. 2012.

[49] J. Gonzalez Hernandez, P. Ruiz-Lapuente, L. Bedin, *et al.*, “Searching for stellar companions of Galactic type-Ia Supernovae with HST and Gaia,” in *Supernova Remnants: An Odyssey in Space after Stellar Death II*, p. 80, June 2019.

[50] R. Di Stefano, “The Progenitors of Type Ia Supernovae. I. Are they Supersoft Sources?,” *Astrophysical Journal*, vol. 712, pp. 728–733, Mar. 2010.

[51] K. Lepo and M. van Kerkwijk, “A Search for Rapidly Accreting White Dwarfs in the Small Magellanic Cloud,” *Astrophysical Journal*, vol. 771, p. 13, July 2013.

[52] T. E. Woods and M. Gilfanov, “He II recombination lines as a test of the nature of SN Ia progenitors in elliptical galaxies,” *Monthly Notices of the Royal Astronomical Society*, vol. 432, pp. 1640–1650, June 2013.

[53] J. Johansson, T. E. Woods, M. Gilfanov, *et al.*, “Diffuse gas in galaxies sheds new light on the origin of Type Ia supernovae,” *Monthly Notices of the Royal Astronomical Society*, vol. 442, pp. 1079–1089, Aug. 2014.

[54] R. P. Olling, R. Mushotzky, E. J. Shaya, *et al.*, “No signature of ejecta interaction with a stellar companion in three type Ia supernovae,” *Nature*, vol. 521, pp. 332–335, May 2015.

[55] M. A. Tucker, B. J. Shappee, P. J. Vallely, *et al.*, "Nebular spectra of 111 Type Ia supernovae disfavour single-degenerate progenitors," *Monthly Notices of the Royal Astronomical Society*, vol. 493, pp. 1044–1062, Mar. 2020.

[56] G. Nelemans, S. Toonen, and M. Bours, "Theoretical Delay Time Distributions," in *Binary Paths to Type Ia Supernovae Explosions* (R. Di Stefano, M. Orio, and M. Moe, eds.), vol. 281 of *IAU Symposium*, pp. 225–231, Jan. 2013.

[57] L.-G. Strolger, S. A. Rodney, C. Pacifici, *et al.*, "Delay Time Distributions of Type Ia Supernovae from Galaxy and Cosmic Star Formation Histories," *Astrophysical Journal*, vol. 890, p. 140, Feb. 2020.

[58] N. Soker, "Supernovae Ia in 2019 (review): A rising demand for spherical explosions," *New Astronomy Review*, vol. 87, p. 101535, Dec. 2019.

[59] E. Bear and N. Soker, "Possible white dwarf progenitors of Type Ia supernovae," *Monthly Notices of the Royal Astronomical Society*, vol. 480, pp. 3702–3705, Nov. 2018.

[60] G. Aznar-Siguán, E. García-Berro, P. Lorén-Aguilar, N. Soker, and A. Kashi, "Smoothed particle hydrodynamics simulations of the core-degenerate scenario for Type Ia supernovae," *Monthly Notices of the Royal Astronomical Society*, vol. 450, pp. 2948–2962, July 2015.

[61] X. Meng and W. Yang, "The birth rate of supernovae from double-degenerate and core-degenerate systems," *Astronomy and Astrophysics*, vol. 543, p. A137, July 2012.

[62] M. Ilkov and N. Soker, "Type Ia supernovae from very long delayed explosion of core-white dwarf merger," *Monthly Notices of the Royal Astronomical Society*, vol. 419, pp. 1695–1700, Jan. 2012.

[63] R. F. Webbink, “Double white dwarfs as progenitors of R Coronae Borealis stars and type I supernovae.,” *Astrophysical Journal*, vol. 277, pp. 355–360, Feb. 1984.

[64] J. Iben, I. and A. V. Tutukov, “Supernovae of type I as end products of the evolution of binaries with components of moderate initial mass.,” *Astrophysical Journal Supplement Series*, vol. 54, pp. 335–372, Feb. 1984.

[65] R. Napiwotzki, C. A. Karl, T. Lisker, *et al.*, “The ESO supernovae type Ia progenitor survey (SPY),” *arXiv e-prints*, p. arXiv:1906.10977, June 2019.

[66] A. Rebassa-Mansergas, S. Toonen, V. Korol, and S. Torres, “Where are the double-degenerate progenitors of Type Ia supernovae?,” *Monthly Notices of the Royal Astronomical Society*, vol. 482, pp. 3656–3668, Jan. 2019.

[67] R. Scalzo, G. Aldering, P. Antilogus, *et al.*, “Type Ia supernova bolometric light curves and ejected mass estimates from the Nearby Supernova Factory,” *Monthly Notices of the Royal Astronomical Society*, vol. 440, pp. 1498–1518, May 2014.

[68] L. R. Yungelson and A. G. Kuranov, “Merging white dwarfs and Type Ia supernovae,” *Monthly Notices of the Royal Astronomical Society*, vol. 464, pp. 1607–1632, Jan. 2017.

[69] Z. T. Kraicheva, E. I. Popova, A. V. Tutukov, and L. R. Iungelson, “Models for the distribution of spectroscopic binaries with respect to mass of the primary, mass ratio, and orbital semiaxis,” *Astronomicheskii Zhurnal*, vol. 56, p. 520, June 1979.

[70] B. J. Barris and J. L. Tonry, “The Rate of Type Ia Supernovae at High Redshift,” *ApJ*, vol. 637, pp. 427–438, Jan 2006.

[71] D. Poznanski, D. Maoz, N. Yasuda, *et al.*, “Supernovae in the Subaru Deep Field: an initial sample and Type Ia rate out to redshift 1.6,” *MNRAS*, vol. 382, pp. 1169–1186, Dec 2007.

[72] C. Frohmaier, M. Sullivan, P. E. Nugent, *et al.*, "The volumetric rate of normal type Ia supernovae in the local Universe discovered by the Palomar Transient Factory," *MNRAS*, vol. 486, pp. 2308–2320, Jun 2019.

[73] R. Kessler, D. Cinabro, B. Bassett, *et al.*, "Photometric Estimates of Redshifts and Distance Moduli for Type Ia Supernovae," *ApJ*, vol. 717, pp. 40–57, Jul 2010.

[74] O. Graur, D. Poznanski, D. Maoz, *et al.*, "Supernovae in the Subaru Deep Field: the rate and delay-time distribution of Type Ia supernovae out to redshift 2," *Monthly Notices of the Royal Astronomical Society*, vol. 417, pp. 916–940, Oct. 2011.

[75] S. A. Rodney, A. G. Riess, L.-G. Strolger, *et al.*, "Type Ia Supernova Rate Measurements to Redshift 2.5 from CANDELS: Searching for Prompt Explosions in the Early Universe," *Astrophysical Journal*, vol. 148, p. 13, July 2014.

[76] B. Flaugher, H. T. Diehl, K. Honscheid, *et al.*, "The Dark Energy Camera," *AJ*, vol. 150, p. 150, Nov. 2015.

[77] H. T. Diehl, Neilsen, R. A. E., Gruendl, *et al.*, "Dark energy survey operations: years 4 and 5," 2018.

[78] J. P. Bernstein, R. Kessler, S. Kuhlmann, *et al.*, "Supernova Simulations and Strategies for the Dark Energy Survey," *ApJ*, vol. 753, p. 152, July 2012.

[79] R. Kessler, J. Marriner, M. Childress, *et al.*, "The Difference Imaging Pipeline for the Transient Search in the Dark Energy Survey," *AJ*, vol. 150, p. 172, Dec. 2015.

[80] R. G. McMahon, M. Banerji, E. Gonzalez, and VHS Collaboration, "First Scientific Results from the VISTA Hemisphere Survey (VHS)," *The Messenger*, vol. 154, pp. 35–37, Dec. 2013.

[81] J. E. Carlstrom, P. A. R. Ade, K. A. Aird, *et al.*, "The 10 Meter South Pole Telescope," *Publications of the Astronomical Society of the Pacific*, vol. 123, p. 568, May 2011.

[82] J. P. Bernstein, R. Kessler, S. Kuhlmann, *et al.*, “Supernova Simulations and Strategies for the Dark Energy Survey,” *Astrophysical Journal*, vol. 753, p. 152, July 2012.

[83] T. M. C. Abbott, F. B. Abdalla, S. Allam, *et al.*, “The Dark Energy Survey: Data Release 1,” *Astrophysical Journal Supplement Series*, vol. 239, p. 18, Dec. 2018.

[84] M. Smith, M. Sullivan, P. Wiseman, *et al.*, “First cosmology results using type Ia supernovae from the Dark Energy Survey: the effect of host galaxy properties on supernova luminosity,” *Monthly Notices of the Royal Astronomical Society*, vol. 494, pp. 4426–4447, Apr. 2020.

[85] E. Bertin and S. Arnouts, “SExtractor: Software for source extraction.,” *Astronomy and Astrophysics, Supplement*, vol. 117, pp. 393–404, June 1996.

[86] D. A. Goldstein, C. B. D’Andrea, J. A. Fischer, *et al.*, “Automated Transient Identification in the Dark Energy Survey,” *Astronomical Journal*, vol. 150, p. 82, Sept. 2015.

[87] D. Brout, M. Sako, D. Scolnic, *et al.*, “First Cosmology Results Using Type Ia Supernovae from the Dark Energy Survey: Photometric Pipeline and Light-curve Data Release,” *Astrophysical Journal*, vol. 874, p. 106, Mar. 2019.

[88] J. Guy, P. Astier, S. Nobili, *et al.*, “SALT: a spectral adaptive light curve template for type Ia supernovae,” *Astronomy and Astrophysics*, vol. 443, pp. 781–791, Dec. 2005.

[89] P. Nugent, A. Kim, and S. Perlmutter, “K-Corrections and Extinction Corrections for Type Ia Supernovae,” *Publications of the Astronomical Society of the Pacific*, vol. 114, pp. 803–819, Aug. 2002.

[90] M. Betoule, R. Kessler, J. Guy, *et al.*, “Improved cosmological constraints from a joint analysis of the SDSS-II and SNLS supernova samples,” *Astronomy and Astrophysics*, vol. 568, p. A22, Aug. 2014.

[91] J. Mosher, J. Guy, R. Kessler, *et al.*, “Cosmological Parameter Uncertainties from SALT-II Type Ia Supernova Light Curve Models,” *Astrophysical Journal*, vol. 793, p. 16, Sept. 2014.

[92] R. Hounsell, D. Scolnic, R. J. Foley, *et al.*, “Simulations of the WFIRST Supernova Survey and Forecasts of Cosmological Constraints,” *ApJ*, vol. 867, p. 23, Nov 2018.

[93] G. Bazin, N. Palanque-Delabrouille, J. Rich, *et al.*, “The core-collapse rate from the Supernova Legacy Survey,” *Astronomy and Astrophysics*, vol. 499, pp. 653–660, June 2009.

[94] F. James and M. Roos, “MINUIT - A SYSTEM FOR FUNCTION MINIMIZATION AND ANALYSIS OF THE PARAMETER ERRORS AND CORRELATIONS,” *Computer Physics Communications*, vol. 10, pp. 343–367, Aug. 1975.

[95] N. Palanque-Delabrouille, V. Ruhlmann-Kleider, S. Pascal, *et al.*, “Photometric redshifts for type Ia supernovae in the supernova legacy survey,” *Astronomy and Astrophysics*, vol. 514, p. A63, May 2010.

[96] R. Kessler, J. P. Bernstein, and D. Cinabro, “SNANA: A Public Software Package for Supernova Analysis,” *PASP*, vol. 121, p. 1028, Sept. 2009.

[97] R. Kessler, D. Brout, C. B. D’Andrea, *et al.*, “First cosmology results using Type Ia supernova from the Dark Energy Survey: simulations to correct supernova distance biases,” *MNRAS*, vol. 485, pp. 1171–1187, May 2019.

[98] D. Brout, D. Scolnic, R. Kessler, *et al.*, “First Cosmology Results Using SNe Ia from the Dark Energy Survey: Analysis, Systematic Uncertainties, and Validation,” *Astrophysical Journal*, vol. 874, p. 150, Apr. 2019.

[99] R. R. Gupta, S. Kuhlmann, E. Kovacs, *et al.*, “Host Galaxy Identification for Supernova Surveys,” *Astronomical Journal*, vol. 152, p. 154, Dec. 2016.

[100] D. Scolnic and R. Kessler, “Measuring Type Ia Supernova Populations of Stretch and Color and Predicting Distance Biases,” *ApJl*, vol. 822, p. L35, May 2016.

[101] L.-G. Strolger, T. Dahlen, S. A. Rodney, *et al.*, “The Rate of Core Collapse Supernovae to Redshift 2.5 from the CANDELS and CLASH Supernova Surveys,” *Astrophysical Journal*, vol. 813, p. 93, Nov. 2015.

[102] J. Guy, M. Sullivan, A. Conley, *et al.*, “The Supernova Legacy Survey 3-year sample: Type Ia supernovae photometric distances and cosmological constraints,” *Astronomy and Astrophysics*, vol. 523, p. A7, Nov. 2010.

[103] J. Guy, P. Astier, S. Baumont, *et al.*, “SALT2: using distant supernovae to improve the use of type Ia supernovae as distance indicators,” *Astronomy and Astrophysics*, vol. 466, pp. 11–21, Apr. 2007.

[104] D. O. Jones, D. M. Scolnic, A. G. Riess, *et al.*, “Measuring the Properties of Dark Energy with Photometrically Classified Pan-STARRS Supernovae. I. Systematic Uncertainty from Core-collapse Supernova Contamination,” *Astrophysical Journal*, vol. 843, p. 6, July 2017.

[105] R. Kessler, B. Bassett, P. Belov, *et al.*, “Results from the Supernova Photometric Classification Challenge,” *Publications of the Astronomical Society of the Pacific*, vol. 122, p. 1415, Dec. 2010.

[106] M. Vincenzi, M. Sullivan, R. E. Firth, *et al.*, “Spectrophotometric templates for core-collapse supernovae and their application in simulations of time-domain surveys,” *Monthly Notices of the Royal Astronomical Society*, vol. 489, pp. 5802–5821, Nov. 2019.